UNIVERSITY OF ULSAN

SCHOOL OF CHEMICAL ENGINEERING

——————————o0o——————————

MASTER'S THESIS

MODIFIED ELECTRONIC STRUCTURE OF ZINC OXIDES FOR PHOTOCATALYTIC HYDROGEN EVOLUTION

Student : **VUONG HOAI THANH**

Student ID : **20205801**

Supervisor : **Prof. Jin Suk Chung, Ph.D**
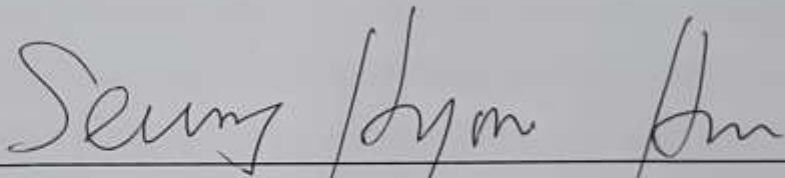
ULSAN CITY, REPUBLIC OF KOREA, MAY 2022

MODIFIED ELECTRONIC STRUCTURE OF ZINC OXIDES FOR PHOTOCATALYTIC HYDROGEN EVOLUTION

This certifies that the thesis of Vuong Hoai Thanh is approved

Committee Chair Professor Won Mook Choi

Committee Member Professor Seung Hyun Hur

Committee Member Professor Jin Suk Chung

Department of Chemical Engineering

Ulsan, Korea

May 2022

ACKNOWLEDGEMENT

ABSTRACT

In this thesis, the concentration was put on the fabrication of ZnO-based heterojunction photocatalysts to improve photocatalytic activities of hydrogen generation from water. The studies have been divided into two parts, including p-n heterojunctions and type II heterojunctions. The mechanism of each type of catalyst under UV and visible light irradiation was clearly illustrated in the thesis.

The first part describes the in-situ synthesis of multicomponent ZnO-based photocatalysts for hydrogen production. The fabricated ZnO coupled with Cu-Cu_2O nanoparticles and modified reduced graphene oxide (mRGO) ameliorated hydrogen production. The simultaneous introduction of mRGO and Cu-Cu_2O enhanced the generation rate of photocatalytic hydrogen to 3085.02 μmol g^{-1} h^{-1} due to significant alteration of the electronic structure. The bandgap energy of the prepared catalysts decreased from 3.2 eV for pristine ZnO to 2.64 eV for a composite containing 15% Cu-Cu_2O. The optimized designated heterostructure efficiently separates photo charge carriers and prevents charge carriers' recombination by accelerating charge transfer with the help of mRGO and metallic Cu and as a result leading to efficient hydrogen yields.

The second part obviously demonstrates the role of EDTA molecules to enhance the photocatalytic activity of CdS/$ZnMn_2O_4$. The composite strongly improved catalytic performance due to the low photo-resistance when bridging EDTA molecules between two materials. Besides that, the optimal composite showed superior hydrogen production at a rate of 26.34 mmol.g^{-1}.h^{-1}. Furthermore, the material possessed better photostability in both acid and basic environments for around 18 h under light

irradiations. This research could be useful to validate the efficacy of organic-inorganic systems for photocatalysts because of the positive effect of organic factors in synthesizing heterojunction photocatalysts, promoting charge transfers, and reducing recombination of electron-hole pairs to increase photoactivity.

TABLE OF CONTENTS

LISTS OF FIGURES

viii

LISTS OF TABLES

ABBREVIATIONS

Abbreviation	Full name
HER	Hydrogen evolution reaction
CB	Conduction band
VB	Valance band
HRPXRD	High-resolution power X-ray diffraction
XPS	X-ray photoelectron spectroscopy
UPS	Ultraviolet photoelectron spectroscopy
AFM	Atomic force microscope
FETEM	Field emission transmission electron microscope
FESEM	Field emission scanning electron microscope
EDS	Energy-dispersive X-ray spectroscopy
DRS	Diffuse reflectance spectroscopy
PL	Photoluminescence

CHAPTER 1: INTRODUCTION

Due to the depletion of conventional energy sources and environmental damage induced by the overuse of coal and petroleum products, the development of environmentally friendly alternative and renewable energy sources has become a primary goal for researchers around the world. Solar energy has attracted interest because of its ubiquity, plenty, and inexhaustibility. Nevertheless, the intermittent nature of sunlight results in the need to store solar energy in other forms. Solar-to-chemical energy conversion can pave the way for a new generation of fuels [1, 2].

In the concept of low-carbon future energy, hydrogen has been stated as an ideal future-fuel gas owing to its precious properties encompassing high energy density, non-toxic gas emission while combustion, and inexpensiveness. Hydrogen can be used in integration with or without fuel cells to generate electricity. The production of hydrogen could be from diverse sources, including water, hydrocarbons, and organic matters. From the literature, various methods to produce hydrogen have been proposed, comprising photocatalysis, electrocatalysis, photo-electrocatalysis, biological methods, and thermal decomposition. Nonetheless, approximately 88 % of hydrogen production these days is from nonrenewable sources, which can negatively influence the goal of sustainable developments. To fulfill the urgent requirement for green hydrogen technologies, water splitting is a promising option because of its environmental friendliness, efficiency, starting materials' abundance, and easy operation [3, 4, 5, 6].

Water splitting via photocatalysis mimics the natural photosynthesis process. Hydrogen evolution reaction (HER) in the presence of nanostructure photocatalysts is one of the popular research subjects in this field. In this reaction, under light irradiation,

the photogenerated electrons in the photocatalyst conduction band migrate to the surface of catalysts and actively participate in the water reduction process [7]. The reaction can be described in several major steps. Firstly, the reactants (H_2O molecules) are absorbed on the surface of catalysts, followed by the generation of electrons and holes from photocatalysts under light irradiation. Subsequently, the photo charge carriers transfer from the bulk to the surface of catalysts where the reaction occurs before hydrogen molecules are released from the surface through the desorption process [8]. Successful commercialization of this process will require low-cost and environmentally friendly photocatalysts with a higher separation rate, greater light absorption, and rapid photo-redox reactions on the surface of catalysts [9].

The ability of zinc oxide (ZnO), an n-type semiconductor, to generate hydrogen under light irradiation has been widely scrutinized due to its electron mobility, but the large bandgap energy at 3.37 eV limits its light absorption [10, 11, 12]. According to preliminary reports, pure ZnO is associated with low photocatalytic yields in both water splitting and decontamination due to rapid electron-hole pair recombination [13]. Photo-corrosion and dissolution of ZnO can also undermine photocatalytic performance [14]. To circumvent these barriers, various techniques have been exploited, including defect engineering [15], doping of other metal and nonmetal elements [14, 16, 17], and coupling ZnO with noble metals such as platinum or with metal sulfides [18, 19]. Chuan Fu Tan et al. reported the preparation of one-dimensional metallic nanocrystals of CuAu with ZnO to enhance photocatalytic properties by directly combining them with plasmonic nanomaterials [20]. Wei Yang Lim et al. developed a heterostructure of $ZnMoS_4$/ZnO/CuS to enhance the photocatalytic-hydrogen production rate by

increasing the light absorption capacity and reducing charge carries recombination. In this study, CuS which was loaded into the system by using the photodecomposition process remarkably boosted charge separation and increased hydrogen evolution rate [21]. Hence, the various ZnO-based heterojunction photocatalysts have been reported previously.

In this thesis, chapter 2 describes more backgrounds of ZnO and ZnO-based heterojunction photocatalysts for hydrogen evolution reactions (HERs) due to the focus of the studies based on ZnO. The influential factors for HERs were also detailed and summarized in the literature. Besides that, heterojunction photocatalytic mechanisms withdrawn from published papers were also included to shed the light on the clear insights to fabricate potential materials.

In chapter 3, the providing lists and synthetic methods for the research in the thesis were provided. There were 24 needed chemicals for two types of synthesized materials. In addition, the photocatalytic studies and materials' characterizations were described in detail.

Following, chapter 4 pictured the simultaneous role of Cu-Cu$_2$O and mRGO to control the bandgap energy of ZnO nanocomposites in which the electronic structures were clearly altered. The research also showed that the photo-corrosion of ZnO in UV light irradiation could have an effect on the materials for a prolonged time using. The p-n heterojunction photocatalytic mechanism was proposed based on the calculation of work function values.

In chapter 5, the demonstration of the spinel material, ZnMn$_2$O$_4$, cooperated with CdS via EDTA bridges to improve the efficiency was reported. The obtained materials

exhibited an adept photo-stability in both acidic and basic environments for 18 h using under visible light irradiations. Moreover, the role of EDTA molecules in the electronic structures of materials was clearly investigated. The dense formation of CdS on the surface of $ZnMn_2O_4$ was mainly responsible for the superior results in hydrogen production efficiency.

Finally, the conclusion and recommendation in chapter 6 depicted the efficiency of heterojunction photocatalysts. The potential materials and their industrial scale could be predicted for the generation of future fuels, hydrogen.

CHAPTER 2: LITERATURE REVIEWS

2.1 Zinc Oxide (ZnO)

Zinc oxide (ZnO), an n-type semiconductor, is created from two elements zinc (2+) and oxygen (2-) with about 230 million tons of zinc and mining areas widely distributed around the world, leading to the inexpensiveness and abundance of this metal oxide. Besides that, the oxide possesses a large bandgap and exciting binding energies at approximately 3.37 eV and 60 m, respectively. Due to the nearly similar properties to TiO_2, ZnO exhibits better photocatalytic activities under UV light irradiation. However, the electron mobility of ZnO is larger than that of TiO_2, which can contribute to the increment of electron transportations and higher quantum efficiencies [22, 23].
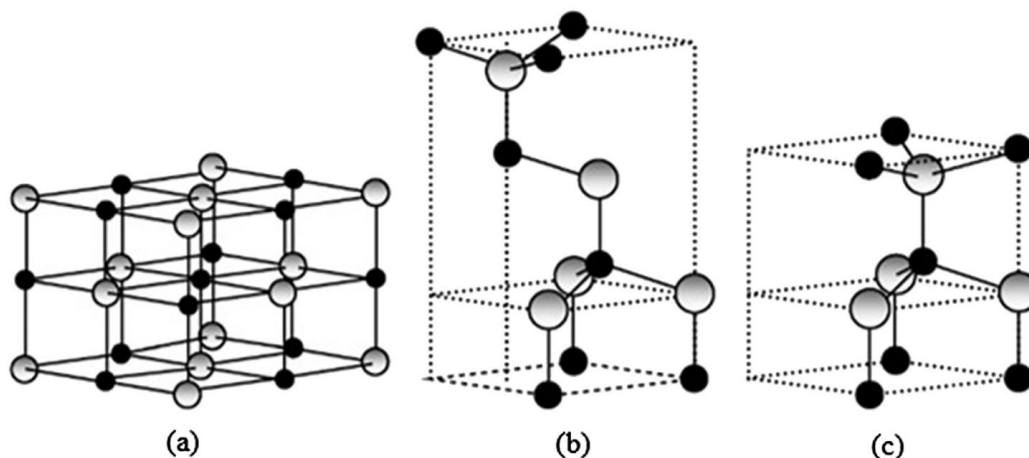
Fig. 2. 1 The rocksalt (a), zincblende (b), and wurtzite (hexagonal) structures model of ZnO [24]

In the chemical structure aspects, ZnO exists in three types of crystallizations including rocksalt, zincblende, and wurtzite, as shown in Fig. 2.1. The former structure is relatively rare because it can be only formed under high pressure. In contrast, the third

structure is most thermodynamically stable at room temperature with the theoretical calculation of two determined lattice parameters a and c individually being 3.25 and 5.2 A° [22, 25].

In addition, it has been stated that due to the large differences in the electronegativity of Zn and O, the valance band (VB) energy was mostly decided by the O 2p orbitals, while the conduction band (CB) energy could be caused by the empty 4 s orbital of Zn and the hybridization of empty s and p orbitals [23]. In the other view, the local density approximation method was used to confirm the range and electronic positions of VB and CB of ZnO. The results showed that the position of VB ranged from -10 to -5 eV corresponding with the Zn 3d orbitals, whereas the CB location was between -5 to 0 eV, which may relate to O 2p levels [26]. The calculated bandgap energy from this measurement was reported around 3.77 eV [27]. From this electronic structure, ZnO shows the broad range of UV light absorption spectrum and various applications such as photocatalysis, light-emitting diodes, photovoltaic cells, or sensors [22].

2.2 ZnO for Photocatalytic Applications

Fig. 2.2 pictured the general information for water splitting reaction from ZnO photocatalysts. As aforementioned, the photocatalytic reaction occurred by following several steps. Firstly, the reaction started when ZnO underwent light irradiation with the photon energy greater than the bandgap energy of the material. At that time, the photoinduced charge carriers appeared, particularly, holes (h^+) at VB and electrons (e^-) at CB. These separated e^- and h^+ reduced and oxidized water into hydrogen and oxygen. However, it is limited to practical applications for the overall water splitting process

because of the rapid recombination of electron-hole pairs from artificial photocatalysts, ZnO, and the inadequate light absorption ability of ZnO from direct sunlight which involves just 4 % of UV source [28]. The other drawback of ZnO was photo-corrosion under light irradiation which would strongly diminish the practical utilization. The problem could mainly prompt by the photoinduced holes with the crystal facets of ZnO, leading to the decomposition of the oxides [29]. The requirements for efficient ZnO-based photocatalysts were needed and various techniques were proposed in the literature, including morphological modifications, metal and nonmetal doping, or coupling with other materials, which will discuss in the next sections.
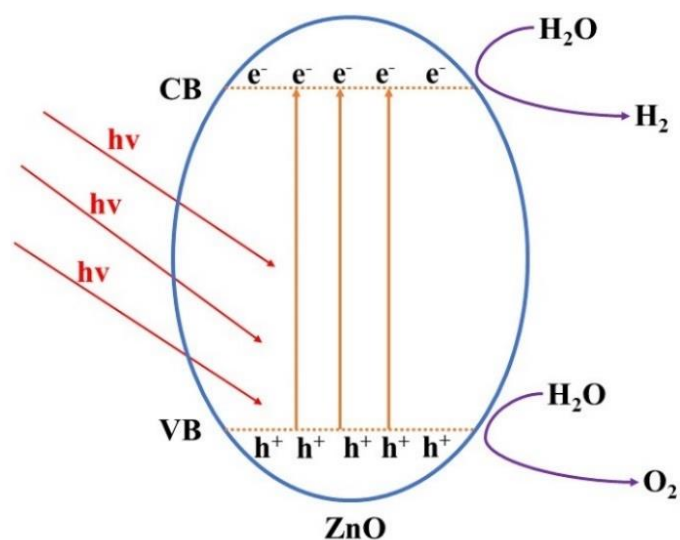
Fig. 2.2 A proposed photocatalytic mechanism of ZnO

2.3 Strategies for Improving Photocatalytic Performances of ZnO

2.3.1 Metal and Nonmetal Doping

Doping the small amount of other elements was implemented in several studies to boost the hydrogen evolution rate. Metallic elements like Lu, Y, Ce, Ga, and Sn doped ZnO were frequently reported [30, 31, 32, 33]. With 5 % of Cu doped

ZnO/Zn$_2$GeO$_4$, hydrogen was produced significantly during the photo-process because Cu particles contributed to a lower recombination rate [34]. Doping Sn^{4+} into ZnO frameworks could improve hydrogen yield owing to a decrease in the photonic gap. In addition, smaller crystallize sizes of Sn doped ZnO generated more active sites compared to pure ZnO [33].

2.3.2 Combining ZnO with other Materials

Di Bao and co-workers generated ZnO/ZnS heterostructured nanorod arrays (ZnO/ZnS HNRAs) by a two-step route. In this study, they investigated the influence of catalyst's amount on hydrogen production. The findings reported that when changing the quality of ZnO/ZnS HNRAs from 0.01 to 0.05 g, the hydrogen evolution experienced a significant increase between 3.6 and 19.2 µmol.h^{-1}. After that, continuously increasing up to 0.2 g of photocatalyst, the rate went up to 15.8 µmol.h^{-1}. This phenomenon was ascribed to maximally absorbed photons while the amount's photocatalyst increases and shielding effects due to the overuse of photocatalysts [35]. Besides, increasing ZnS nanolayers and decreasing particle sizes of ZnS could also lead to the enhancement in hydrogen generation rate. It has been attributed to vacancy defects when an amount of ZnS increased, resulting in facilitating charge carrier separation [36]. Previously, Aiping Wu et al. developed ZnO-dotted porous ZnS cluster microspheres with Pt-free to photo-produce hydrogen. The results proposed that dotting ZnO not only creates efficient electron-hole pair separation but also provides adequate active photocatalytic sites to form hydrogen [37]. Juan Wang and his cooperators fabricated rGO decorated 3D ZnO for this application. In their study, rGO plays a pivotal role as electron acceptors, promoting charge separation and transportation.

However, the excessive amount of rGO could blame for decreasing in hydrogen production yield due to its shielding effects [38].

2.4 Influential Factors for Photocatalytic Hydrogen Evolutions

2.4.1 Effect of Cocatalysts

Nobel metals such as Pt were frequently used as co-catalysts to enhance catalytic efficiency because of promoting the separation of photoexcited electrons and holes. It has been believed that a load of Pt on nanoparticles could increase the range of light absorption [39]. ZnO-CdS@Cd cooperating with Pt as co-catalysts at different percentages involving 0, 1, 2, 3, 5, 8 wt% was reported by Xuewen Wang and his colleagues. With 3 % of Pt loading, 1.92 mmol.h^{-1} of hydrogen was recorded in this study [40]. Additionally, Rimple Kalia and his group observed a similar trend for their hydrogen evolution photocatalysts. At first, the loading of Pt on the surface of nano-catalysts could invigorate the electron-hole pair separation process. Nonetheless, the further growth of Pt concentration leads to the reduction in catalytic activities due to downing the exposed surface with light [41]. Hongchen Yang et al. reported the cooperation of Au and ZnO/CN for visible-light-driven hydrogen evolution. According to the finding, Au nanoparticles act as a sensitizer for creating hot electrons providing extra electrons for ZnO under light illumination, which could produce hydrogen from water [42]. Rh was exploited as a co-catalyst in another study. Even though the catalytic efficiency of hydrogen production rose when incorporating Rh into photocatalysts, this metal was unstable and changed into an oxide phase after 8 h reaction [43].

2.4.2 Effect of Sacrificial Agents

Sacrificial agents have been applied to trap the photoinduced charge carriers to enhance charge separation and improve photocatalytic hydrogen evolution. Significant attention in the field of sacrificial agents for hydrogen production has been paid to carbon-organic compounds, especially for alcohol such as methanol or ethanol. These agents possess simple structures, easily understand reaction mechanisms, and environmentally mineralize with less hazardous products. It can act as a hole-scavenger to suppress the electron-hole pair recombination process [44]. Irshad Ahmad and co-authors tested their photocatalysts in the presence of glycerol and ethanol [30, 45]. In the case of glycerol, it has been inferred that the holes from the valance band of nano-catalysts react with H_2O to generate hydroxyl radicals which continuously interact with glycerol molecules to produce protons. Such protons participated in the hydrogen evolution process by the reduction of electrons [30]. Other authors used formaldehyde that was oxidized to generate H_2 and $HCOO^-$ during the photoinduced process [42]. Na_2S was reported with the ability to improve hydrogen generation rate on account of increasing oxidation-reduction reaction as well as diminishing photo-corrosion [46]. Another common sacrificial agent is triethanolamine (TEOA) which was marked by the consumption of holes and the prevention of forming oxygen [47].

2.5 Research Objective

The overall goal of the research was to improve the photocatalytic hydrogen evolution of ZnO in which different materials were used to adjust the electronic structure in the photocatalyst. The research concentrated on synthesizing the

heterojunction photocatalysts and consisted of two parts based on a p-n heterojunction

photocatalyst and a type II heterojunction photocatalyst.

CHAPTER 3: EXPERIMENTAL

3.1 Materials

The chemicals used in the thesis are shown in Table 3.1.

Table 3.1 Lists of chemicals

No.	Chemicals	Formula	Physical State	Purity	Origin
1	Zinc acetate dihydrate	$Zn(CH_3COO)_2.2H_2O$	Solid	98%	Sigma
2	Copper acetate monohydrate	$Cu(CH_3COO)_2.H_2O$	Solid	98%	Sigma
3	Cadmium acetate dihydrate	$Cd(CH_3COO)_2.2H_2O$	Solid	98%	Sigma
4	Manganese (II) acetate tetrahydrate	$Mn(CH_3COO)_2.4H_2O$	Solid	99%	Sigma
5	Ammonium hydroxide solution	NH_4OH	Liquid	28-30%	Sigma
6	Platinum (IV) chloride	$PtCl_4$	Solid	96%	Sigma
7	Disodium dihydrogen ethylenediaminetetraacetic acid	$C_{10}H_{14}O_8N_2Na_2.2H_2O$	Solid	99.5%	Junsei
8	Oxalic acid	$C_2H_2O_4$	Solid	$< 99.5\%$	Kanto
9	Thioacetamide	C_2H_5NS	Solid	98%	Wako
10	N, N-dimethylformamide	C_3H_7NO	Liquid	99.5%	Daejung
11	Eosin Y	$C_{20}H_6Br_4O_5Na_2$	Solid	-	Daejung

12	Graphene Oxide	-	Solid	-	Standard Graphene
13	Sodium sulfide pentahydrate	$Na_2S.5H_2O$	Solid	97%	Daejung
14	Sodium sulfite	Na_2SO_3	Solid	97%	Kanto
15	Zinc oxide	ZnO	Solid	< 100 nm	Sigma
16	Titanium dioxide	TiO_2	Solid	< 100 nm	Sigma
17	Methanol	CH_4O	Liquid	99.5%	Daejung
18	Ethanol	C_2H_6O	Liquid	99.5%	Daejung
19	Lactic acid	$C_3H_6O_3$	Liquid	85%	Kanto
20	Ascorbic acid	$C_6H_8O_6$	Solid	99%	Sigma
21	Thionyl chloride	$SOCl_2$	Liquid	99%	Daejung
22	N-methyl-2-pyrrolidone	C_5H_9NO	Liquid	99.5%	Daejung
23	Melamine	$C_3H_6N_6$	Solid	99%	Daejung
24	N-N-dicyclohexylcarbodiimide (DCC)	$C_{13}H_{22}N_2$	Liquid	98%	Daejung

3.2 Preparation of Cu-Cu$_2$O/ZnO/mRGO (CZG)

3.2.1 Synthesis of Carboxylic Rich Graphene Oxide (GO-COOH)

Firstly, 1 g of GO was dispersed in 1000 ml DI water with sonicating at a high power for 1 hour to obtain the homogeneous solution. Subsequently, 10 g of oxalic acid

(OA) was added to the above solution with overnight stirring. The dispersion was filtered and washed several times before redispersing in 1000 mL of DI water.

3.2.2 Synthesis of Amine Functionalized GO-COOH (GO-NH₂)

GO-NH$_2$ was prepared via amidation reactions between -COOH groups in GO-COOH and -NH$_2$ groups in melamine. The as-prepared GO-COOH (1 mg/mL) was stirred in the three-neck round bottom flask with 50 mL of SOCl$_2$ under reflux conditions overnight to activate -COOH groups before adding the aqueous melamine solution (20 mg/mL) and maintaining the reaction conditions for 7h at 70 ℃. The product, referred to as GO-NH$_2$, was collected and washed to remove un-reacted substances, followed by dispersing in 1000 mL of NMP.

3.2.3 Synthesis of Eosin Y Functionalized GO-NH$_2$

500 mg of DCC and 500 mg of Eosin Y were added to the as-dispersed GO-NH$_2$ in NMP. The mixture was stirred at 60 ℃ for 48h before filtrating, rinsing with DI water, and drying at 80 ℃ in the oven. The functionalized product was referred to as EY-GO.

3.2.3 Synthesis of Cu-Cu$_2$O@ZnO/mRGO

Modified graphene oxide was synthesized according to methods previously described with minor modifications [48]. A solvothermal method was used to prepare Cu-Cu$_2$O@ZnO p-n heterojunctions. Briefly, a suitable amount of Cu(CH$_3$COO)$_2$.H$_2$O was added to a 100 mL Teflon-lined stainless-steel autoclave containing 2.77 g of Zn(CH$_3$COO)$_2$.2H$_2$O and 80 mL of GO–eosin Y in DMF (0.2 mg/mL). The autoclave was then sealed and heated at 200 °C for 48 h. The products were labeled as xCZG,

with x being the theoretical percentage of copper in the ZnO. Comparison samples included TiO_2, ZnO from synthesis (ZnO_s), commercial ZnO (ZnO_c), Cu-Cu_2O, Cu-Cu_2O/mRGO (CG), ZnO/mRGO (ZG), and 10Cu-Cu_2O@ZnO (10CZ). These samples were synthesized with the same procedure. The general preparation procedure of the photocatalysts is depicted in Fig. 2.1.
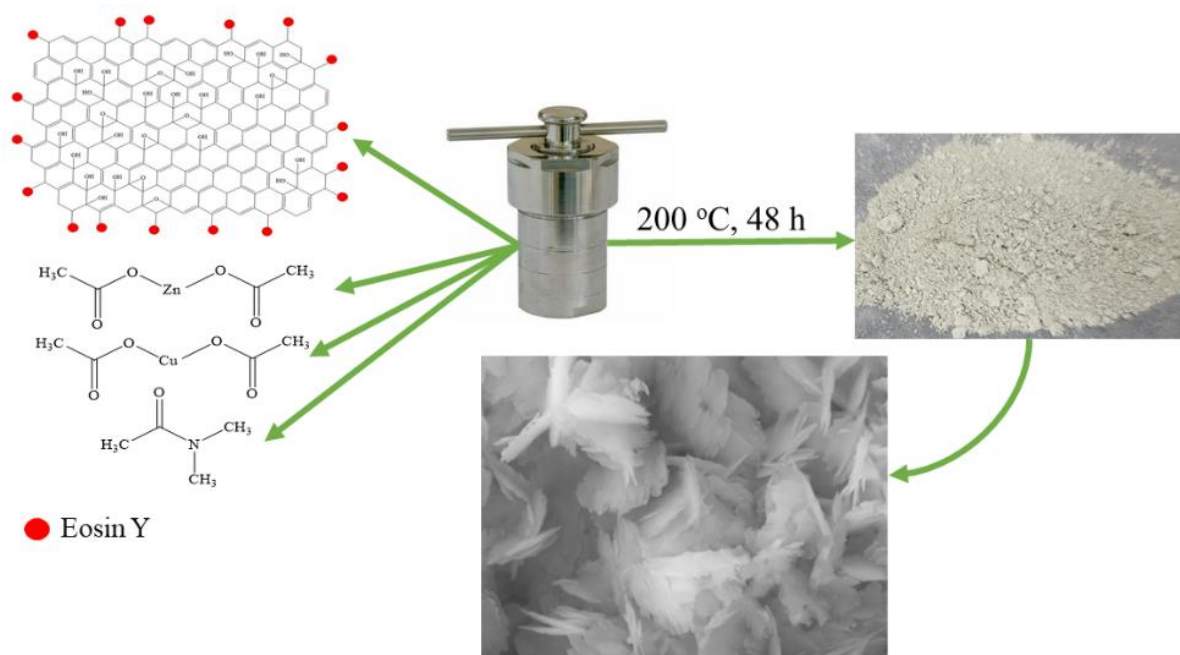
Fig. 3.1 A general synthetic scheme for Cu-Cu_2O@ZnO/mRGO

3.2.4 Photocatalytic Studies

50 mg of photocatalysts was dispersed into 100 mL of deionized water containing 0.35 M Na_2S and 0.25 M Na_2SO_3 in a photoreactor with 3 h illumination by an ultraviolet (UV) Osram Ultra Vitalux 300 W light source. The produced gases were detected by an online gas chromatograph equipped with a thermal conductivity detector using an argon gas carrier. First, the system was purged with argon for 30 min to

eliminate any remaining gas. The light was then turned on and the amount of hydrogen was measured at regular intervals of 30 min.

3.3 Preparation of CdS-EDTA/ZnMn$_2$O$_4$ (ZMCE)

3.3.1 Synthesis of CdS

The (CH$_3$COO)$_2$Cd. 2H$_2$O (0.04 mol) was dissolved in methanol (320 mL) in a 500 mL beaker under vigorous stirring until a clear solution was obtained. Afterward, NH$_4$OH was quickly injected into the solution to attain a final pH of over 10. Thioacetamide (0.1 mol) was subsequently poured into the prepared solution and continued stirring for a few minutes to form a yellowish-green complex. Then, 80 mL of the complex solution was transferred into a 100 mL Teflon-lined stainless-steel autoclave, which was thoroughly sealed and heated at 120 °C for 8 h in an oven. After naturally cooling down to ambient temperature, the precipitates were collected and washed with methanol, deionized water, and ethanol several times before overnight drying in an oven at 80 °C to obtain CdS.

3.3.2 Synthesis of ZnMn$_2$O$_4$/CdS$_E$ (ZMCE)

1 g of synthesized CdS nanosheets was dispersed into deionized water (400 mL) and sonicated for 1 h. After that, 0.5 g of Na-EDTA was added to the suspension with stirring vigorously for 24 h at 80 °C. Followingly, the suitable amounts of (CH$_3$COO)$_2$Zn.2H$_2$O and (CH$_3$COO)$_2$Mn. 2H$_2$O was added to the mentioned solution and continuously stirred for 6 h at the same temperature. Finally, 2 g of oxalic acid was introduced to the above mixture under overnight stirring at 80 °C. The product was collected, washed, and dried in an 80 °C oven. 1.5 g of the as-prepared materials were

calcined at 200 °C for 2 hours in the furnace with a ramping rate at 5 °C min^{-1}. The final powders were labeled as xZMCE, with x presenting the calculated weight of $ZnMn_2O_4$ in the sample. For comparisons, CdS, CdS-EDTA (CdS$_E$), and $ZnMn_2O_4$ were synthesized with the same procedure. The general preparation procedure of the photocatalysts is depicted in Fig. 2.2.
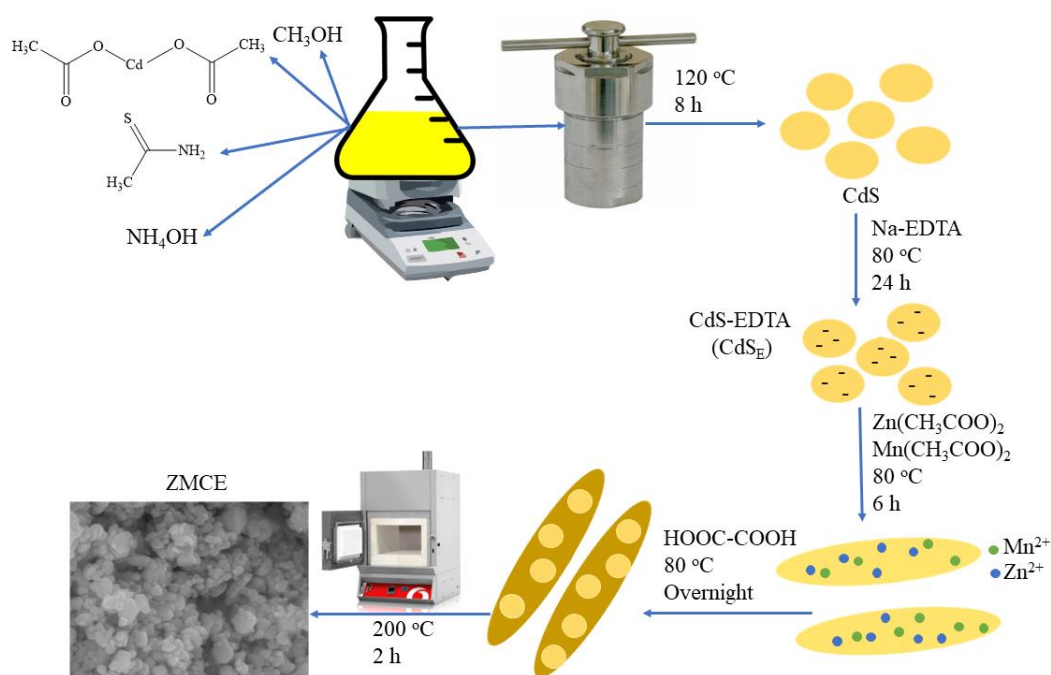
Fig. 3.2 A general scheme of prepared CdS$_E$/$ZnMn_2O_4$

3.3.3 Photocatalytic Studies

The photocatalytic hydrogen evolution reaction was conducted in a quartz flask. Particularly, 10 mg of as-prepared photocatalysts and 0.5 mL of aqueous PtCl$_4$ solution (0.54 mg/mL) were dispersed into 100 mL DI water. A flow of highly purified Ar was blown into the system to eliminate other gases, as well as the photodecomposition process, was performed under the irradiation of a 300 W merry lamp as a solar simulator

for 30 min. Subsequently, Na_2S and Na_2SO_3 were poured into the flask to obtain the final concentration at 0.35 and 0.25 M, respectively. The system was blown with Ar for another 30 min to remove the remaining gases inside the reactor before the hydrogen production was undertaken. To determine the generated hydrogen content, the online gas chromatography equipped with a thermal conductivity detector was applied. The hydrogen amount was repeatedly measured with an interval time of 30 min.

3.4 Characterizations

High-resolution powder X-ray diffraction (HRPXRD), and X-ray photoelectron spectroscopy (XPS) were utilized to determine the chemical and phase composition of the composites. Raman and Fourier-transform infrared spectroscopies were used to validate the composites' chemical functional groups. Morphological analysis and elemental distributions were conducted by the employment of atomic force microscopy (AFM), field-emission transmission electron microscope (FE-TEM), and a field-emission scanning electron microscope (FESEM) coupled with energy-dispersive X-ray spectroscopy (EDS). Zeta potential values were carried out by a zeta potential analyzer (Zetasizer Nano ZS, Malvern Panalytical). The Brunauer-Emmett-Teller analysis was used to determine the surface areas of the materials via a QUADRASORB SI Surface Area and Pore Size Analyzer. To study the electronic structure of the composites, XPS-valance band (XPS-VB) and ultraviolet photoelectron spectroscopy (UPS) were applied to characterize the valance band edge and work function. Electrochemical impedance spectroscopy (EIS) measurements were implemented by an electronic workstation with the use of a calomel electrode as a reference electrode, and a Pt wire as a counter electrode. Besides that, an ultraviolet-visible-near-infrared with

18

diffuse reflectance spectroscopy (UV-Vis-DRS), photoluminescence (PL) spectroscopy, and time-resolved photoluminescence (TRPL) spectroscopy were used to confirm optical properties of the materials.

CHAPTER 4: BANDGAP CONTROL OF ZINC OXIDES COMPOSITING WITH COPPERS, COPPER OXIDES, AND MODIFIED REDUCED GRAPHENE OXIDES

4.1 Introduction

Although ZnO-based photocatalysts can improve hydrogen production yields compared with pristine oxides, almost rapid charge recombination continues and reduces efficiency. To address this issue, composite materials containing graphene or reduced graphene oxide (RGO) have been widely studied. The incorporation of p-type RGO and ZnO forms a p-n heterojunction capable of efficient charge separation with narrow bandgap energy. The RGO acts as an electron acceptor that stores electrons from the ZnO conduction band during illumination, decomposing water into hydrogen on the RGO surface [49]. The presence of graphene (RGO) can reportedly improve light absorption capacity and accelerate the transport of photoinduced charges [50]. Furthermore, RGO, which can participate directly in redox reactions, causes a beneficial effect on heterostructure photocatalysts as macromolecular surfactants for dispersing metal oxides, maximizing their active surface area [51]. In addition, eosin Y has been cited as an effective dye photosensitizer for hydrogen photocatalytic systems using ZnO due to its effective light absorption [52]. Anchoring eosin Y on an RGO structure may offer the combined advantages of improved charge separation and migration in photocatalysts due to the unique electronic property associated with RGO and dye photosensitizers [48]. Previous studies suggest that an eosin-Y/RGO-based system can suppress photoinduced electron-hole pair recombination of photocatalysts [53]. Jin and

his co-workers observed the same results in which eosin Y was used to promote light absorption and accelerate the hydrogen rate [54].

Table 4.1 Summary of photocatalytic hydrogen evolution from literature and this study

Photocatalyst	Light source	Sacrificial agents	Hydrogen evolution rate ($\mu mol.g^{-1}.h^{-1}$)	Reference
ZnO	A 300W UV light	Na_2S	1059.69	This study
5CZG		Na_2SO_3	3085.2	
ZnO	A 300 W Xe lamp	Na_2S	294.44	[55]
Cu@Cu$_2$O/ZnO		Na_2SO_3	1472.2	
N-ZnO	A 300 W Xe lamp	Na_2S	9836	[56]
N-ZnO/g-C$_3$N$_4$		Na_2SO_3	18836	
ZnO	A 300 W Xe lamp	TEOA	501.9	[47]
ZnO/SrTiO$_3$			16006.12	
ZnO/ZnS	A 350 W Xe lamp	Glycerol	384.000	[35]
ZnO	A 300 W Xe lamp	Na_2S	88.7	[57]
		Na_2SO_3		
MoS$_2$-rGO/ZnO	A 300 W Xe lamp	Na_2S	288	[58]
		Na_2SO_3		

Ni-ZnO/rGO	A 300 W Xe lamp	Na_2S $C_6H_{15}NO_3$ Na_2SO_3	1.4	[59]
CuS-ZnO/rGO/CdS	A 300 W Xe lamp	Na_2S Na_2SO_3	1073	[60]
B/CuO/ZnO	A 500 W Xe lamp	Na_2S Na_2SO_3	933	[14]
ZnO@ZnS	A 150 W Xe lamp	Na_2S	126.18	[61]
ZnO ZnO@CuS	A 450 W Xe lamp	Na_2S Na_2SO_3	287.96 10113.59	[62]
ZnO ZnO/rGO	A 300 W Xe lamp	Na_2S Na_2SO_3	279.4 648.1	[38]

Inspired by the preliminary research, the research fabricated Cu-Cu_2O@ZnO-anchored modified RGO (mRGO) using a facile solvothermal method. Compared with the studies listed in Table 4.1, the composite materials demonstrated outstanding photocatalytic activity, possibly due to the synthetic method in which an organic solvent acts as a precursor, leading to the special morphology and also an optimized designated heterostructure. With the efficient charge carrier separation and transfer in the as-prepared p-n heterojunction structure of Cu-Cu_2O@ZnO, and the ability of mRGO to facilitate charge carrier transfer and decrease recombination rate by establishing a ternary heterostructure, photocatalytic hydrogen generation improved, and the

22

optimized sample showed the hydrogen production rate of 3085.02 µmol.g^{-1} .h^{-1} in 3 h illumination. The data validated our hypothesis that the electrons flow from Cu-Cu$_2$O to ZnO before reaching mRGO to reduce water. A possible photocatalytic mechanism was proposed using band energy calculations and ultraviolet photoelectron spectroscopy (UPS) that support the feasibility of p-n heterojunctions and their further applications.

4.2 Results and Discussion

4.2.1 Photocatalytic Hydrogen Evolution Performances
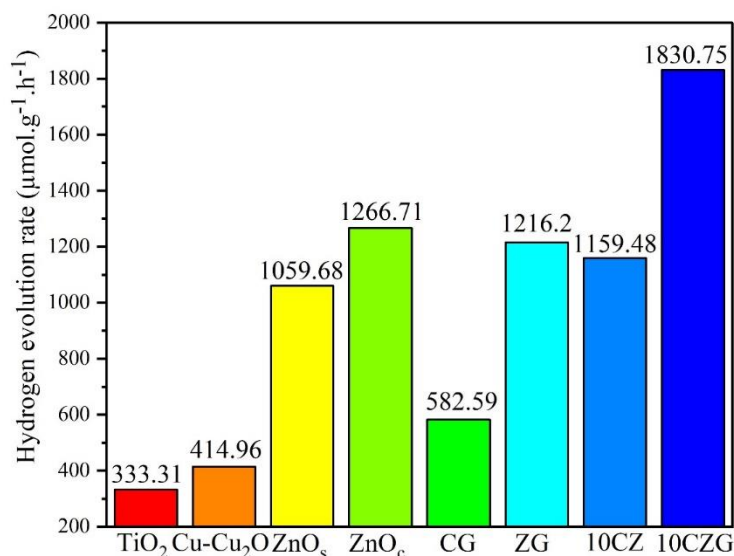
Fig. 4.1 Photocatalytic hydrogen evolution of the as-prepared photocatalysts

Fig. 4.1 provides empirical data on photocatalytic hydrogen evolution from different catalysts in a mixture of Na$_2$S and Na$_2$SO$_3$ as the sacrificial electron donor under UV irradiation. The highest hydrogen rate under light irradiation, 1830.75 µmol .g^{-1}.h^{-1}, was obtained from 10CZG — approximately 4.4, 1.7, and 1.6 times as that of pristine Cu-Cu$_2$O, pristine ZnO, and 10CZ, respectively. Pure oxides, TiO$_2$, Cu-Cu$_2$O,

ZnO$_c$, and ZnO$_s$ exhibited low photocatalytic activity due to the rapid charge carrier recombination. Besides, grafting Cu-Cu$_2$O with ZnO (Cu-Cu$_2$O@ ZnO) enhanced the process slightly. This grafting creates a heterojunction structure that slows down photoinduced charge carriers' recombination [64]. Moreover, introducing mRGO to the pure ZnO or Cu$_2$O is also investigated. The samples consisting of Cu$_2$O/mRGO (CG) and ZnO/mRGO (ZG) depicted a higher hydrogen evolution rate than that of single materials of Cu$_2$O and ZnO, respectively. By introducing eosin-Y/RGO (mRGO) into the framework, the evolution rate was ameliorated due to the facilitated charge transfer property. As a result, integration between the ternary structure of Cu-Cu$_2$O, ZnO, and mRGO could lead to a strong increase in hydrogen production.
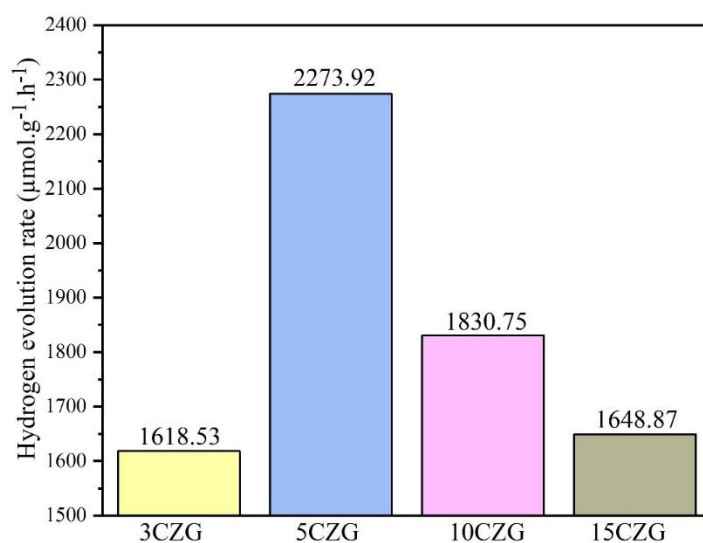
Fig. 4.2 The effect of copper oxide on the photocatalytic activity of the composites

The hydrogen evolution results in Fig. 4.2 demonstrated that an appropriate amount of Cu-Cu$_2$O in the catalyst is the key factor that controls the photocatalytic performance. To optimize the theoretical amount of copper, various samples with different copper values were prepared. As can be seen in Fig. 4.2, the quantity of

produced hydrogen experienced a growth when the copper content rose from 3% to 5%. However, a continuous increase in the proportion of copper caused a decrease in the hydrogen production rate. As expected, the copper content in the form of Cu-Cu$_2$O arranges a suitable p-n heterojunction with ZnO/mRGO which can effectively promote light-harvesting ability and reduce charge carrier recombination in the electronic structure [65, 66]. However, it can be inferred that the overloading of copper can induce the shielding effects in the catalysts, resulting in a decrease in the evolution rate [67]. The BET results from Table 4.2 showed that the overloading of copper content prompted the decrease in the active surface area of the materials.
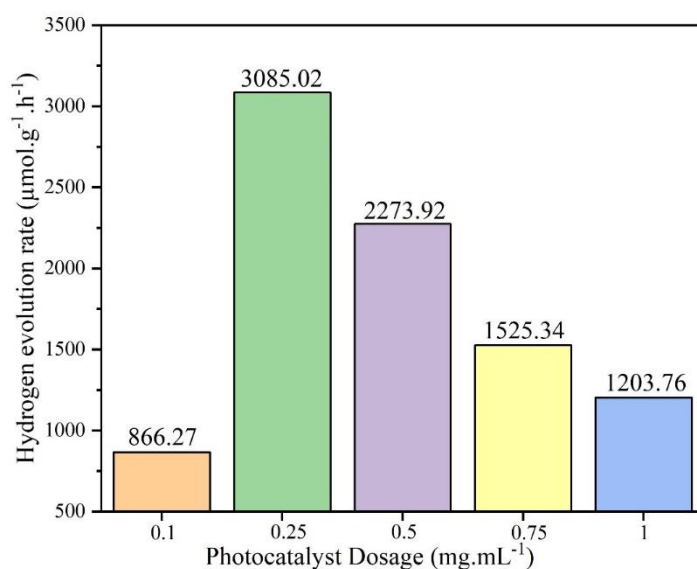
Fig. 4.3 Effect of the amount of 5CZG on hydrogen production

The amount of photocatalyst is a crucial parameter for generating hydrogen through a photocatalytic water-splitting process. In Fig. 4.3, the hydrogen production yield is recorded utilizing various quantities of 5CZG (the optimized ternary structure), ranging from 0.1 to 1 mg.mL^{-1}. Loading of 0.25 mg.mL^{-1} produced the highest hydrogen evolution rate, with the value of 3085.02 µmol.g^{-1}.h^{-1}. A similar trend was previously

reported [13]. This can be explained by the lack of active photocatalytic sites with a small amount of catalyst and shielding effects for the light absorption with overloaded photocatalyst amount in the solution [68]. Hence, the optimum amount of the photocatalyst in this study was approximately 0.25 mg.mL^{-1}.
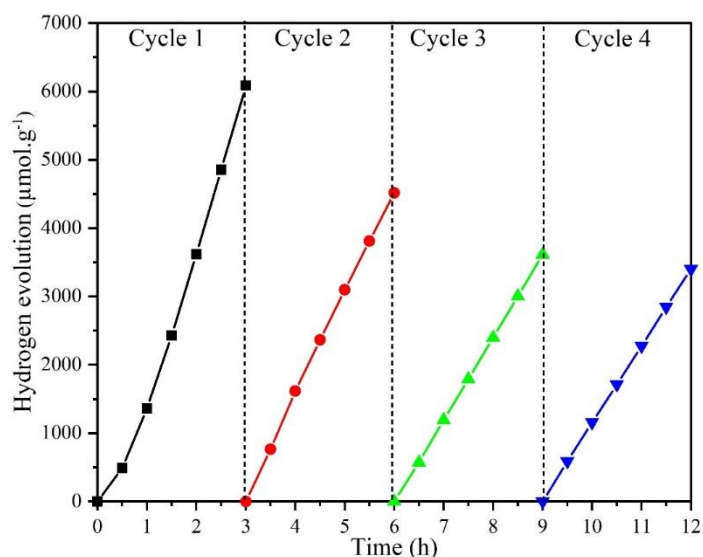
Fig. 4.4 The stability test for 5CZG after four cycles with the addition of sacrificial agents at the end of each cycle

ZnO-based photocatalysts generally suffer from photo-corrosion during the light illumination process. Hence, the photostability investigation of the prepared ZnO-based heterostructure is critical. As shown in Fig. 4.4, the photostability of the as-prepared catalyst (5CZG) was tested for four cycles. The same amounts of sacrificial agents were added after each cycle. The highest hydrogen production yield was obtained in the first cycle before the decrease which was observed in the second cycle from the second cycle an almost stable activity was obtained for the other cycles. The photo-corrosion of ZnO happens because of the holes (h$^+$) production under light irradiation. The produced holes

have enough electrochemical potential to attack the ZnO structure and dissolve in the reaction medium that was shown in Equation (4.1).

$$ZnO + h^+ \longrightarrow Zn^{2+} + H_2O \hspace{4cm} (4.1)$$
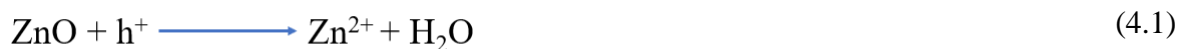
An almost stable photocatalytic activity after the first run suggests that the formation of some trap sites like Zn^{+2} and oxygen vacancies in the ZnO structure probably can act as the recombination centers for the produced holes and decrease the photo corrosion rate drastically. According to the data, the photocatalyst was relatively stable after 4 cycles of hydrogen photo-production. This result was similar to those of previous studies of ZnO-based photocatalysts [69].

4.2.2 Morphological Analyses

Non-hydrolytic reactions that use alcohol as a source of oxygen to form metal oxides have been described in many research papers. Ketones and aldehydes have been also frequently employed as oxygen-supplying agents to support the formation of metal oxides since the examples of titania were reported [70]. As a non-aprotic solvent with high polarity, DMF can act as a reagent due to the presence of a carbonyl group. Synthesis of ZnO using DMF has been reported in published papers. As the higher viscosity of DMF compared with water created a hindrance, a higher temperature was required to induce adequate mobility of Zn^{2+} in the solution [71]. The mechanism of this reaction involved aldol condensation when two carbonyl constituents interacted with each other to eliminate water [72, 73]. It can be assumed that DMF was deprotonated and then combined with zinc or copper to form an enolate complex. This was followed by attacks on other DMF species through aldol condensation to produce

Zn-OH or Cu-OH that then decomposed into ZnO or Cu-Cu$_2$O at high temperatures. The other oxygen-supplying agent was mRGO due to hydroxyl and carboxylic groups on the structure. These oxygens also contribute through a solvothermal process, with metal oxides decorating their planar surface. This chemical reaction can be expressed in equation (3). Furthermore, DMF can partly reduce Cu^{2+} ions into metallic copper which was proved by XRD spectra. That phenomenon was reported in preliminary studies in which DMF can play as a reducing agent for the formation of Ni^{2+}, Co^{2+}, and Ag$^+$ into metal nanoparticles via the oxidative reaction of DMF to carboxylic acid [74]. However, the formation of metallic zinc could not be observed in the work, indicating the insufficient reducing ability of DMF to reduce Zn^{2+} ions to metallic Zn.
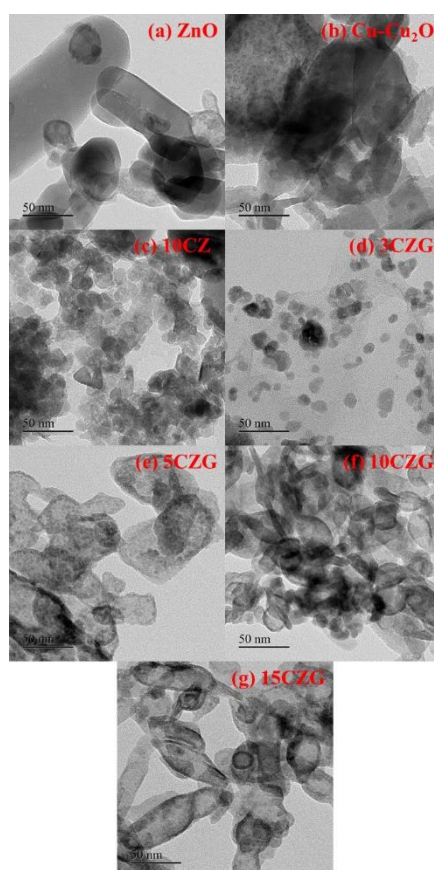
Fig. 4.5 FETEM images of the photocatalysts

$$\text{Zn acetate} + \text{Cu acetate} + \text{DMA} \xrightarrow{200\ ^{\circ}\text{C},\ 48\ \text{h}} \text{Cu-Cu}_2\text{O@ZnO} + \text{By Products} \qquad (4.2)$$
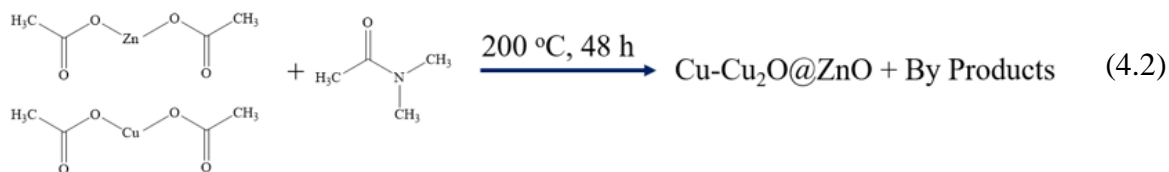
Table 4.2 BET surface are results

Sample	Surface Area (m²/g)	Pore Volume (cm³/g)	Pore Size (nm)
ZnO	27.93	0.083	9
Cu-Cu₂O	31.96	0.399	17
10CZ	49.54	0.108	2
3CZG	33.04	0.286	9
5CZG	48.61	0.754	29
10CZG	52.36	0.862	29
15CZG	38.48	0.586	29

Fig. 4.6 supplies FE-SEM images of the as-prepared materials with various shapes that are consistent with FE-TEM results in Fig. 4.5. While the pristine ZnO had a grain-like shape, Cu-Cu₂O appeared in a defective spherical structure with strong agglomeration. Cooperation between ZnO and Cu-Cu₂O is evident in Fig. 4.6c and d. The addition of mRGO with a Cu^{2+} content of greater than 5% led to the formation of striking flower-like crystals. The flower petals produced by mRGO with 15% of Cu^{2+} can be seen in Fig. 4.6g. Following the generation of the first ZnO nuclei without mRGO, they rapidly agglomerated to form larger grain-like crystals. The phenomenon

was similar to the formation of Cu-Cu$_2$O nanoparticles as well as the composite of ZnO and Cu-Cu$_2$O, in which Cu-Cu$_2$O anchored on the ZnO surfaces formed a core-shell structure. The mRGO acted as a substrate as oxygen groups on its structure induced a pinning force to circumvent agglomeration of ZnO nuclei, allowing for the fabrication of nano-flowers by continuously grafting Cu-Cu$_2$O into ZnO surfaces [75]. The other factor that had an impact on the construction of nano-flowers was the content of Cu^{2+}. While a Cu^{2+} content of 3% was not sufficient to form nano-flowers in the presence of mRGO, at 5% to 15%, uninterrupted decoration of Cu-Cu$_2$O on grain-like ZnO formed nano-petals. Because the reaction occurred in multiple dimensions, flower-like crystals were produced. Fig. 4.6h represents the morphology of the sample after light irradiation. It is clear that the agglomeration in the composites occurred, indicating the decrease in photocatalytic activity because it can reduce the active sites.
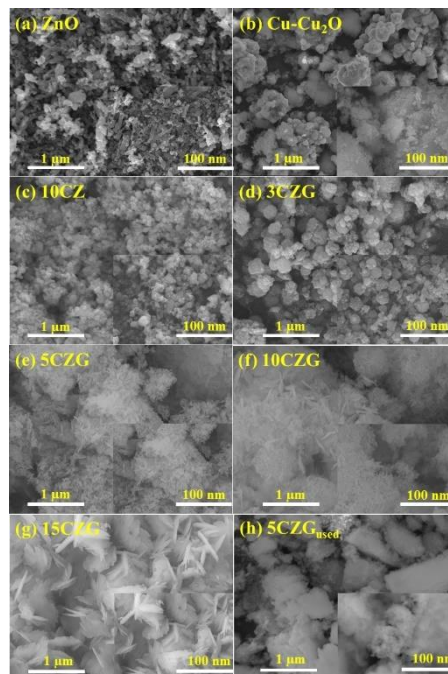
Fig. 4.6 FE-SEM images of the photocatalysts

4.2.3 XRD and Compositional Analyses
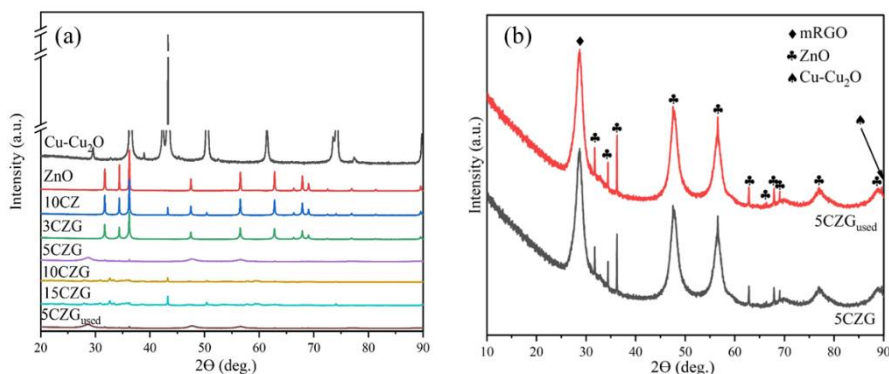
Fig. 4.7 XRD patterns of the photocatalysts

HRPXRD analysis provided insights into the crystallization structure of the materials. Fig. 4.7 shows the crystal structures of obtained materials. The HRPXRD patterns of 5CZG, and 5CZG after reaction (5CZG$_{used}$) are shown in Fig. 4.7b. From the diffraction patterns, the peaks at 31.72° (100), 34.38° (002), 36.22° (101), 47.48° (102), 56.54° (110), 62.78° (103), 66.36° (200), 67.92° (112), 69.06° (201), 76.88° (202), and 89.56° (203) were in a close agreement with the standard peaks of a hexagonal wurtzite structure of ZnO (JCPDS card No. 36-1451) [76]. While the different peaks at 29.53° (110), 36.41° (111), 42.27° (200), 52.47° (211), 61.37° (220), and 77.38° (220) can be ascribed to the face-centered cubic Cu_2O (JCPDS card No. 78-2076). Also, the peaks located at 43.30° (111), 50.43° (200), and 74.10° (220) go to metallic copper (JCPDS card No. 04-0836).

Interestingly, similar diffraction XRD patterns appeared for 5CZG$_{used}$, suggesting the crystallite structure stability of the as-prepared photocatalyst. The lattice fringe spacing of 0.25 and 0.28 nm shown in Fig. 4.8 corresponds to (111) for Cu_2O and (110) for ZnO, respectively, which was consistent with XRD results. The mapping

images for 5CZG and 5CZG$_{used}$ from FE-SEM images in Fig. 4.8 provide the distribution of each element and suggest the uniform loading of Cu on ZnO surfaces. Additionally, the mapping image for 5CZG$_{used}$ gives evidence of sulfurization after light illumination, in which sulfur has densely distributed and becomes uniform on the catalysts' surfaces. However, the XRD results indicated the successful synthesis of metal oxides via a solvothermal method, with the stronger intensity seen in the XRD patterns validating the higher crystallinity of the oxides.
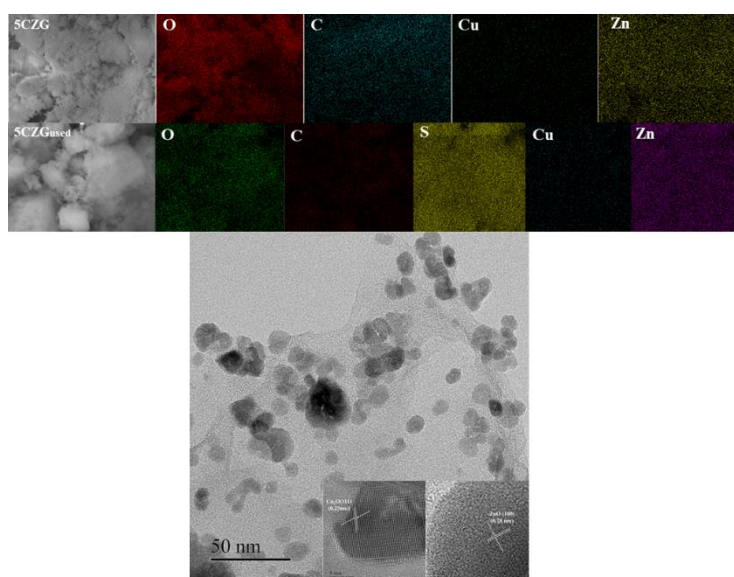
Fig. 4.8 FETEM image and selected area electron diffraction patterns of 5CZG and EDS-mapping images of 5CZG and 5CZG$_{used}$

4.2.4 Raman and FTIR Analyses

Fig. 4.9a provides the Raman spectra of ZnO and 5CZG samples Zinc sublattice vibrations in ZnO were marked with a peak near 100 cm^{-1}, while the typical peak for the hexagonal phase of ZnO at 437 cm^{-1} can be assigned to oxygen oscillation corresponding to the E$_2$ model [77, 78, 79]. The peak at 330 cm^{-1} corresponds to the

multi-phonon mode of ZnO, and the peak at 1155 cm^{-1} belongs to E$_1$ symmetry in the 2LO mode [80]. For the spectra of Cu-Cu$_2$O, the small peak near 109 cm^{-1} is associated with an inactive Raman mode for perfect Cu$_2$O crystals [81]. The two main Raman features of mRGO were also observed in the composite materials due to the presence of peaks around 1333 and 1587 cm^{-1}, correlating with the G and D bands, respectively [48]. In general, the as-prepared photocatalysts consisted of all the single recorded peaks in both ZnO and Cu-Cu$_2$O, suggesting the formation of designated heterojunctions. In further analysis of the 5CZG$_{used}$ photocatalyst after irradiation, the peaks at 330 and 437 cm^{-1} became more prominent, indicating higher crystallinity due to the UV light used to synthesize the metal oxides [82].
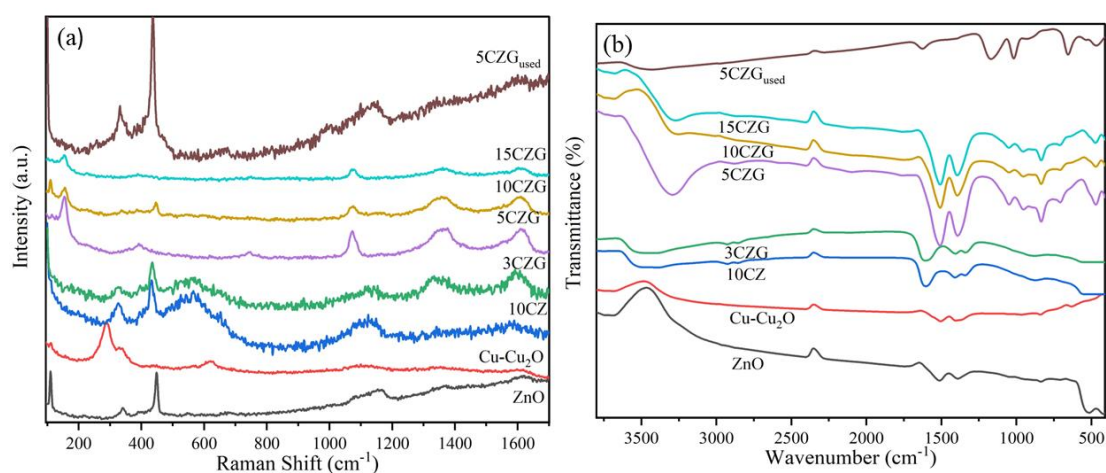
Fig. 4.9 Raman spectra (a) and FTIR spectra (b) of photocatalysts and 5CZG after hydrogen photocatalytic reaction

The chemical composition and bonding vibrations in materials can be determined by FTIR analysis [83]. The FTIR spectra of the studied materials are presented in Fig. 4.9b. Previous studies determined that the peaks near 500 and 628 cm^{-1} were due to the oscillation of the Zn-O stretching band with oxygen vacancies in the

ZnO and Cu-O bond, respectively [84, 85]. As a result, the presence of sharp peaks confirmed the formation of metal oxides via solvothermal synthesis. In the analysis of 5CZG and 5CZG$_{used}$, it is clear that the broad peak at 3300 cm^{-1} corresponds to O-H vibrations which can be from some remaining OH groups at the mRGO surface, as well as intercalated moisture in the structure. The three peaks at approximately 1580, 1045, and 1384 cm^{-1} are associated with C-O-C, C-O from the epoxide, and C=O from carboxylic groups on planar graphene [86, 87]. Three other peaks at 941, 821, and 705 cm^{-1} observed only in 5CZG may correlate with the stretching vibrations of the Zn-O bond [88]. This may be a function of intrinsic interactions between the content of Cu^{2+} and the addition of mRGO, which were responsible for defect sites in the photocatalysts due to co-effects between mRGO, Cu-Cu$_2$O, and ZnO [89]. All the peaks for 5CZG$_{used}$ appeared at nearly the same positions, except for the peaks at 1150 and 1122 cm^{-1}, which were assigned to ZnS and S-O impurities due to the production of sulfur species during the light irradiation [90, 91].

4.2.5 XPS Results

The chemical states of the elements at the surface of the prepared catalysts were investigated using XPS analysis. Fig. 4.10a supplies the XPS survey spectra of 5CZG and 5CZG$_{used}$. The survey XPS spectra comprised peaks of Zn 2p, Cu 2p, O 1s, and C 1s with no S 2p peaks before illumination. Two distinct peaks at 1044.6 and 1021.5 eV corresponding to Zn 2p$_{1/2}$ and Zn 2p$_{3/2}$ in the core level XPS spectrum of Zn, Fig. 4.10b, validate the presence of zinc at the surface of the catalyst, respectively [10]. Based on the positions of the obtained Zn peaks and their energy difference because of the spin-orbit effect, we determined that zinc species are in the form of Zn^{2+}.
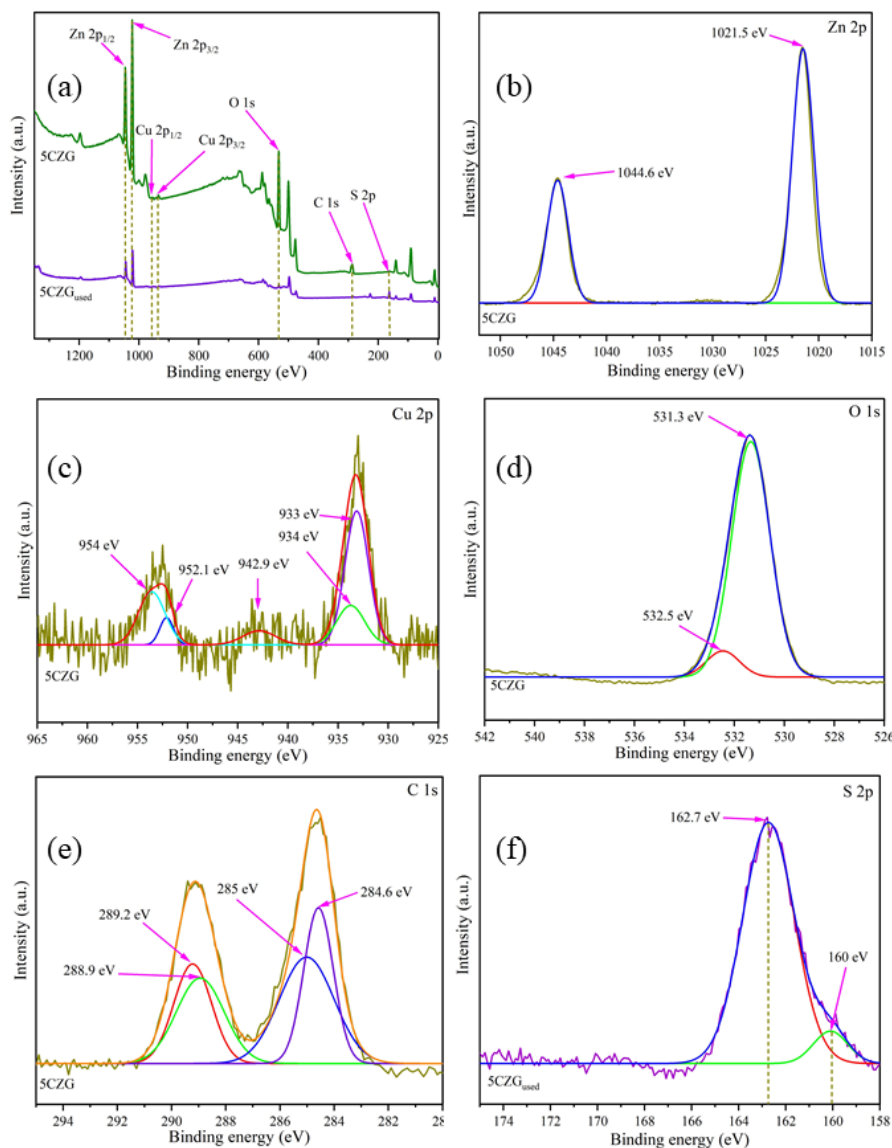
Fig. 4.10 XPS spectra of as-prepared photocatalysts: survey spectra of 5CZG and 5CZG$_{used}$ (a); the deconvolution spectra of containing elements in 5CZG (b-e), the deconvolution spectra of S 2p from 5CZG$_{used}$ (f)

In the O1s core level spectrum, Fig 4.10d, the shoulder peak at 532.5 eV indicates chemisorbed oxygen from hydroxyl groups on the surface of materials, whereas the deconvoluted peak at 531.3 eV can be attributed to the lattice oxygen of ZnO and Cu$_2$O [92]. Furthermore, the Cu 2p core-level spectra, Fig. 4.10c, confirm the presence of Cu in the sample in the form of Cu$^+$ and Cu^0 [93, 94]. Four fitting peaks

consisting of 284.6, 285, 288.9, and 289.2 eV for the C 1s spectrum in Fig. 4.10e were sequentially assigned to sp^2 C-C, sp^3 C-C, C=O, and O-C=O belonging to the presence of mRGO [95, 96]. After exposure to light, the formation of metal sulfide was detected, as shown in Fig. 4.10f, with two deconvolution peaks of sulfide at 160 and 162.7 eV, corresponding to the S $2p_{3/2}$ and S $2p_{1/2}$ states, respectively, and indicating the photo-corrosion of ZnO-based photocatalysts during the reaction [97].

4.2.6 UV-Vis-DRS Results

It is essential to determine the bandgap energy of materials in photocatalysis and its effect on photocatalytic activity. To excited electron-hole pairs, the photon energy should be equal to or greater than the bandgap energy of the materials. In the case of ZnO, the bandgap is the energy caused by the transition of the electron from an O 2p to Zn 3d orbital [77]. A Kubelka-Munk model, which offers a high degree of accuracy, was used to compute the bandgap energy of materials by diffuse reflectance spectra. The plots in Fig. 4.11 were exported according to a previous study based on the relationship between $(F(R)h\upsilon)^2$ and $h\upsilon$ using Equation (4.3) [98]:

$$\left(\log\left(\frac{1}{R}\right)\frac{\ln(10)}{l}h\upsilon \right)^r = B(h\upsilon - E_g) \tag{4.3}$$

where R is the reflectance value, l is the width of materials (cm), B is a constant, E_g is the bandgap energy (eV), h is the Planck's constant, υ is the frequency (s^{-1}), and r is equal to 2 for direct bandgaps.

The obtained bandgap energies for pristine ZnO and Cu-Cu$_2$O are 3.2 and 1.84 eV, respectively which are comparable to previously published values [77]. Integration

of ZnO with Cu-Cu$_2$O decreased the bandgap energy slightly to 3.16 eV, and a significant diminution in bandgap energy to 2.73 eV was recorded in the presence of mRGO for 10CZG. When the effect of Cu-Cu$_2$O was investigated, paralleling the incremental change in the percentage of copper in the composites, the bandgap energy values decreased from 3.1 to 2.64 eV. Although the bandgap energy contributed primarily to photoactivity, useful conclusions cannot be drawn without determining the positions of the valance band (VB) and conduction band (CB) in the redox potential scale [98].
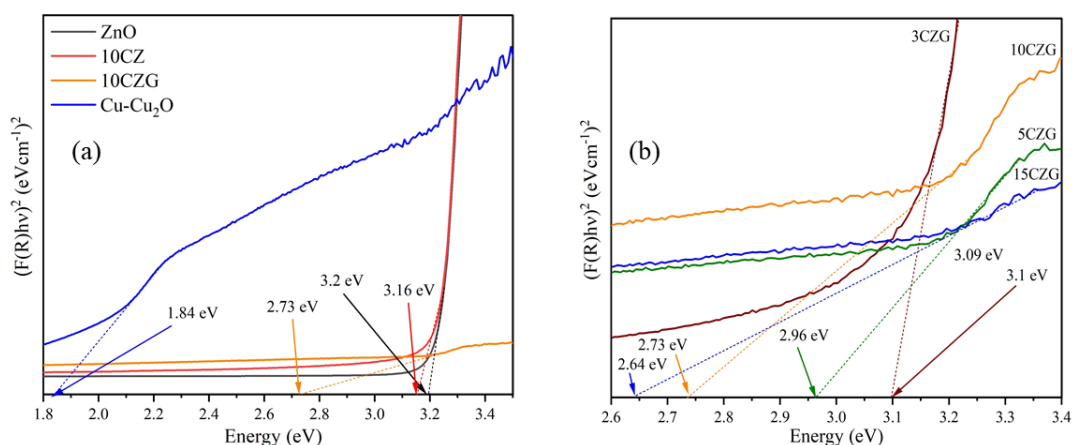
Fig. 4.11 The optical bandgap energy of as-synthesized photocatalysts from UV-DRS analysis

4.2.7 PL Results

Defects also contribute to photocatalytic performance and play a critical role in photocatalysis because they relegate electron-hole pair recombination and act as trapping states through the alteration of the band structure. Photoluminescence (PL) spectroscopy is a powerful tool for determining the defects in the photocatalyst structure. The emission of the electrons from higher potentials to lower potentials can

be recorded through the steady-state PL spectra [98]. The lower intensity in PL spectra reportedly represents a quenched photoinduced charge recombination which promotes photocatalytic efficiency [99]. As can be seen in Fig. 4.12a, a strong emission peak near 390 nm for pure ZnO decreased in intensity after cooperating with Cu-Cu$_2$O and mRGO. By increasing the Cu-Cu$_2$O content in the samples, the intensity of the peak shows much more reduction, indicating the formation of appropriate p-n heterojunction that enhances photocatalytic activity by preventing charge carrier recombination. However, noting the intensity versus wavelength in PL spectra is not sufficient to conclude. Previously, Mooney and Kambhampati proposed the transformation of PL spectra into two important subtitles [100]. To fully analyze PL spectra, the wavelength should first be converted into energy by Equation (4.4). Second, it is crucial to preserve the emission spectra area during wavelength transformation, leading to conversion of the intensity by Equation (4.5):

$$E = \frac{hc}{\lambda} \qquad (4.4)$$

$$I = I_o \frac{hc}{E^2} \qquad (4.5)$$

where I and I_o are the respective intensity per energy and the intensity per wavelength, h is Planck's constant, c is the photon velocity (nm), λ is the wavelength (nm), and E is photon energy (eV).
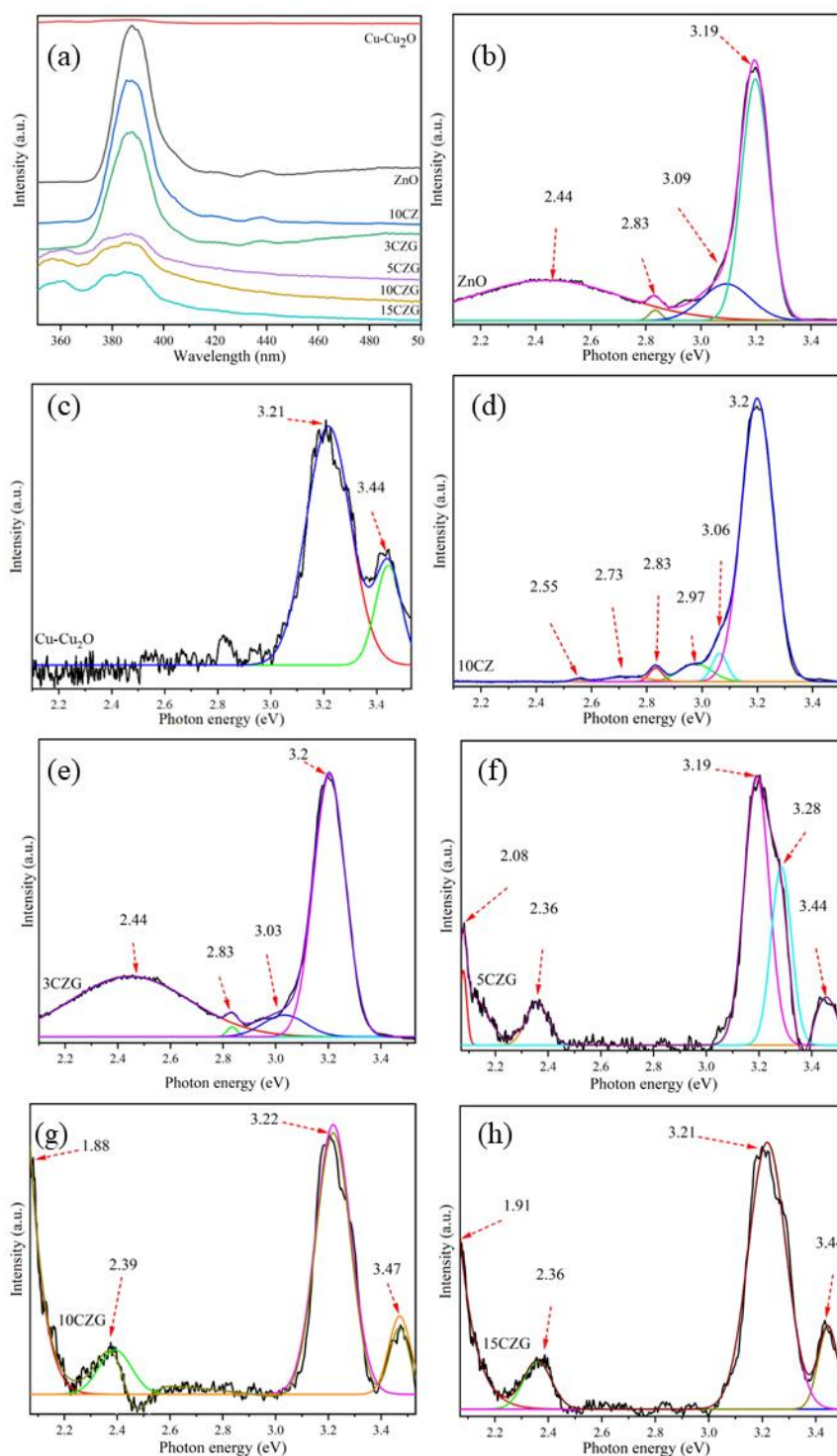
Fig. 4.12 Photoluminescence spectra of the as-prepared photocatalysts (a); the deconvoluted spectra of the PL peaks based on energy transformation plots for ZnO, Cu-Cu2O, 10CZ, 3CZG, 5CZG, 10CZG, and 15CZG (b-h)

Fig. 4.12b to 4.12h indicates the intensity versus the photon energy converted from the PL spectra, using Gaussian peak-fitting to determine the differences in band alignment of each composite. A strong peak in all samples near 3.2 eV in the UV region corresponds to the near-band-edge of the materials and as a result of charge recombination [101, 102, 103]. The peaks associated with Cu-Cu$_2$O, 5CZG, 10CZG, and 15CZG at approximately 3.44 eV can be attributed to band-edge emissions [104, 105]. The results were similar to those of previous studies that used copper acetate as a precursor [106]. While the peaks at 1.9 eV for 5CZG and 10CZG, and 2.07 for 15CZG were ascribed to interstitial oxygen defects in ZnO induced by the monovalent vacancies of zinc and oxygen, the green peaks near 2.4 eV for ZnO, 3CZG, 5CZG, 10CZG, and 15CZG were associated with anti-site oxygen defects [101, 107]. The blue peaks near 2.83 and 3.03 eV observed in ZnO, 10CZ, and 3CZG were preliminarily explained by intrinsic defects or/and copper impurities. According to previous reports, the blue emissions can be attributed to the transition of electrons from the bottom of the CB to zinc vacancies and from the interstitial zinc level to the top of the VB [108].

4.2.8 UPS Results

To determine the VBM of the synthesized materials, UPS was employed. The respective VBMs of ZnO, Cu-Cu$_2$O, 10CZ, 3CZG, 5CZG, 10CZG, and 15CZG (Table S1) were 2.06, 1.2, 1.71, 2.31, 2.66, 1.98, and 2.2 eV. Accordingly, the CB for ZnO, Cu-Cu$_2$O, 10CZ, 3CZG, 5CZG, 10CZG, and 15CZG computed by Equation (4.6) was positioned at −1.14, −0.64, −1.45, −0.79, −0.3, −0.75, and −0.44 eV:

$$E_c = E_v - E_g \qquad\qquad (4.6)$$

where E_c and E_v are the CB and VB energies (eV), respectively.

Table 4.3 Electronic properties of photocatalysts

Sample	E_g (eV)	E_v (eV)	E_c (eV)	E_{cutoff}	W(eV)
ZnO	3.2	2.06	-1.14	16.71	4.51
Cu-Cu$_2$O	1.84	1.20	-0.64	16.75	4.47
10CZ	3.23	1.71	-1.45	16.8	4.42
3CZG	3.10	2.31	-0.79	16.72	4.5
5CZG	2.96	2.66	-0.3	16.77	4.45
10CZG	2.73	1.98	-0.75	16.8	4.42
15CZG	2.64	2.20	-0.44	16.82	4.4

The changes in work function were conducted by UPS measurements. The work functions of ZnO, Cu-Cu$_2$O, 10CZ, 3CZG, 5CZG, 10CZG, and 15CZG were calculated by Equation (4.7) [109]:

$$W = h\nu - E_{cutoff}$$ (4.7)

where hv and E_{cutoff} are the photon energy for He I, 21.2 (eV), and the binding energy (eV), respectively.

The calculated work function results for all samples could be found in Table 4.3. The calculated work functions for ZnO and Cu-Cu$_2$O were 4.51 and 4.47 eV. It has been stated that electrons will move from the lower work function semiconductor to the higher one to facilitate the equilibrium of Femi levels. Based on this evidence, it can be

suggested that the as-prepared catalysts are type II heterojunctions (p-n junction) [98, 110, 111]. The mechanism of the junction formation and photocatalytic H_2 production has been discussed in detail in the next part. Fig. 4.13 shows the electronic band structures of the as-prepared photocatalysts. Amalgamating ZnO, Cu-Cu$_2$O, and mRGO have had a strong control on the alteration of the materials' band energies which could be responsible for the enhancement in photocatalytic performance by efficient separation and transfer of electron-hole pairs and retarding charge carriers' recombination.
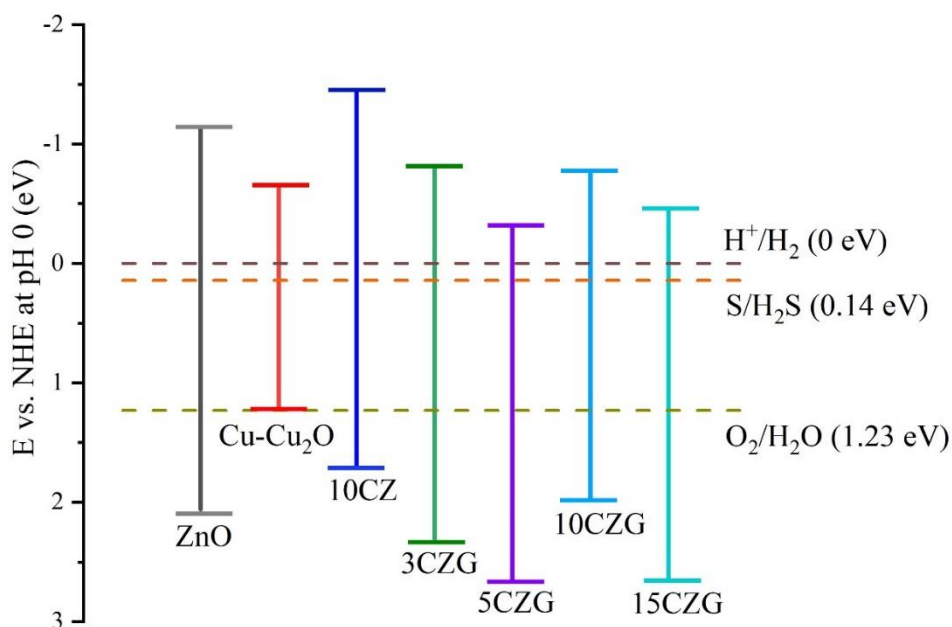
Fig. 4.13 Energy band structure of as-prepared materials

4.2.9 Photocatalytic Mechanism

Based on the above results, a possible p-n heterojunction formation and H_2 evolution reaction mechanism are proposed in Fig. 4.14. The band structures of Cu-Cu$_2$O and ZnO before contact and after contact are shown in Fig. 4.14a. The alignment

before contact was drawn based on the XPS/UPS data and bandgap measurements. There is a p-type (Cu_2O) and n-type (ZnO) semiconductors. The band structure of these two semiconductors will reconfigure after contact (p-n junction) as the fermi levels of Cu_2O and ZnO try to be aligned, Fig. 4.14a. The third part of the heterostructure is mRGO which has a metal-like character and a Schottky junction will appear at the joint position of the semiconductor and mRGO in Fig. 4.14b. Upon the light irradiation, the electrons and holes will appear in both Cu_2O and ZnO conduction band and valence band. Based on the formed p-n junction the electrons will flow from the Cu_2O conduction band to the ZnO conduction band and the holes will flow from the ZnO valence band to the Cu_2O valence band. The mRGO interlayer does not contribute to the generation of photoexcited electron-hole because it does not have an energy gap. mRGO as a connector can show two roles, the first one is as the mediator between Cu_2O and ZnO which will accelerate the electron flow and hence, enhance the electron/hole separation, the second with its metal-like character formed a Schottky junction with ZnO and Cu_2O, and transfer electrons and holes from the ZnO conduction band and Cu_2O valence band to the catalyst/electrolyte interface, respectively and provide a direct path for charge carriers. The formation of metallic Cu in the Cu_2O structure will also accelerate electron and hole transfer in the formed junctions and as a result decrease charge recombination. The charge carriers at the catalyst interface will participate in reduction and oxidation reactions. As a result, the photogenerated electron-hole pairs are effectively separated, which is crucial for the enhancement of photocatalytic activity. The combined effects of the introduction of mRGO sheets and

the formation of the p-n heterojunction contribute to the enhancement in the efficiency of photocatalytic hydrogen production.
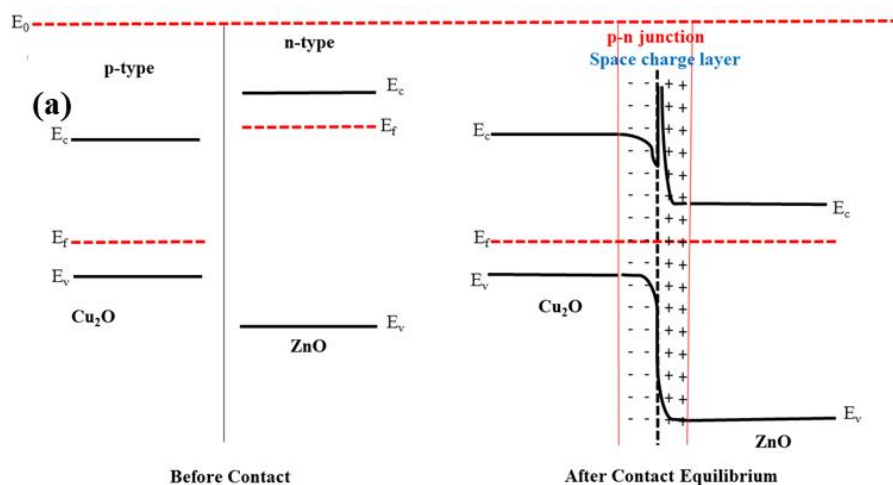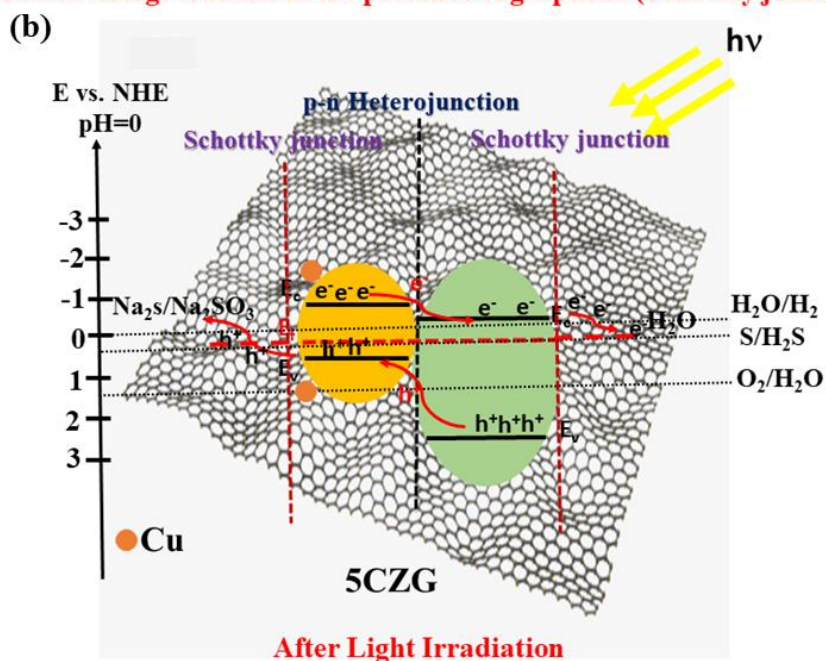
Fig. 4.14 A possible mechanism of photocatalytic hydrogen evolution

4.3 Conclusion

In this study, Cu-Cu_2O@ZnO has been attached to mRGO via a one-pot facile solvothermal synthesis procedure. The bandgap energy of materials is significantly

44

adjusted by controlling the content of Cu-Cu$_2$O in the structure via the formation of a suitable p-n heterojunction with ZnO. The formation of the p-n heterojunction increases light-harvesting capability and decreases charge carrier recombination. Moreover, the introduction of mRGO to the structure as an electron acceptor and mediator increase charge carrier transfer in the heterostructure and retard the charge carriers' recombination and, as a result, enhance photocatalytic water reduction reaction (H$_2$ production). The spontaneous formation of metallic Cu in the Cu$_2$O structure can also promote charge transfer and reduce the recombination rate. These findings should help in the design of the new material for the practical utilization of photocatalysts.

CHAPTER 5: MODIFIED ELECTRONIC STRUCTURE OF CADMIUM SULFIDES AND ZINC MANGANESE OXIDES VIA EDTA BRIDGES

5.1 Introduction

The other approach to improving photocatalytic hydrogen evolution rate was cooperation to form heterojunctions with metal sulfides. Various materials were proposed and reported in the literature. Qingrui Luan and co-authors fabricated the Z-scheme heterojunction based on 2D ZnS@ZnO photocatalysts. The results showed that with a high order of ZnO and disorder of ZnS the separation efficiency rate increased over 7.2 times than that of pure ZnO via photocurrent measurements [112]. In the other research, the utilization of organic compounds like EDTA molecules to connect two semiconductors was also carried out. The EDTA bridges between CdS and g-C_3N_4 were recorded by some scientists. They reported that the cooperation of EDTA molecules in the system can significantly enhance photocatalytic activity due to the efficient separation of photoinduced charge carriers as well as the suitability of the redox potentials. This molecule also helped to control the morphology in nanostructures, sticking two materials to boost charge transfer between them [113]. Besides that, various metal oxides - metal sulfides systems exhibited their efficiency as reported in Table 5.1.

In this chapter, inspired by other research, the fabrication of CdS/$ZnMn_2O_4$ via EDTA bridges was reported. The results exhibited the important role of EDTA molecules in reducing photo-resistance, accelerating the charge transportations, and

leading to a superior hydrogen generation rate. This also indicated that EDTA can prolong the lifetime of an electron in which the reduction of water into hydrogen was more efficient. From electronic structural analyses, the type II heterojunction mechanism was proposed for this material. Apart from the other mechanisms, from this catalyst, the synthesis of type II heterojunction photocatalysts validated the efficiency with the ease of the synthesized process, advancing the potential for a larger scale in the near future.

Table 5.1 Summary of photocatalytic hydrogen evolution from literature and the work

Photocatalysts	Light Source	Sacrificial agents	Hydrogen evolution rate $(mmol.g^{-1}.h^{-1})$	Reference
Pt-CdS-EDTA@ZnMn$_2$O$_4$	A 300 W Mercury Lamp	Na$_2$S Na$_2$SO$_3$	26.34	This study
CdS@Zn-C	LED	Na$_2$S Na$_2$SO$_3$	6.6	[114]
Pt-CdS-EDTA/ Graphene Hydrogel	A 500 W Xenon Lamp	Na$_2$S Na$_2$SO$_3$	1.56	[115]
CdS/Au/ZnO	A 300 W Xenon Lamp	Na$_2$S Na$_2$SO$_3$	0.608	[116]
Pt-CdS Quantum Dots/ZnO	A 225 W Xenon Lamp	Na$_2$S Na$_2$SO$_4$	22.12	[117]
Pt-ZnO/CdS	A 300 W Xenon Lamp	Na$_2$S Na$_2$SO$_3$	3.87	[118]

Ascorbic Acid-CdS/ZnO	A 300 W Xenon Lamp	Na_2S Na_2SO_3	268.5	[119]
MnO_x/CdS	LED	Na_2S Na_2SO_3	4.7	[120]
Pt-MnO_2/CdS	A 300W Xenon Lamp	Na_2S Na_2SO_3	3.94	[121]
$Zn_{0.5}Cd_{0.5}S$/MnO_2	LED	Na_2S Na_2SO_3	24.56	[122]
ZnO-WS_2@CdS	A 300W Xenon Lamp	Lactic Acid	15.12	[123]

5.2 Results and Discussion

5.2.1 Photocatalytic Hydrogen Performances
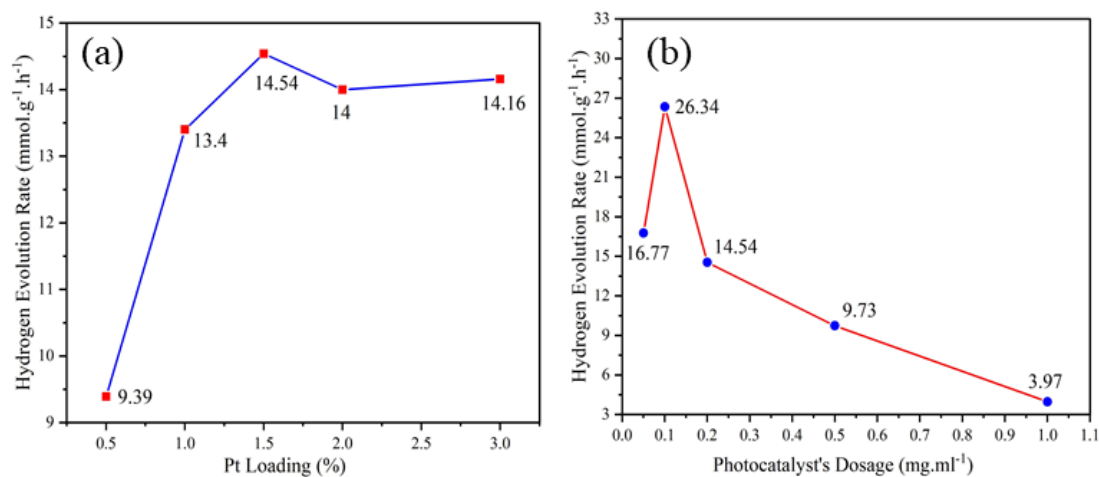
Fig. 5.1 Photocatalytic hydrogen evolution performances: (a) Effect of the amount

of Pt loading on ZMCE; (b) Effect of ZMCE's dosage

The utilizations of noble metals such as Pt as a cocatalyst to increase

photocatalytic performances were frequently reported. It has been stated that Pt can

48

improve visible light absorption efficacy because of the surface plasmon resonance effect and playing as an electron sink in which the charge recombination can be suppressed [124]. The effect of the amount of Pt loading on the surface of ZMCE with the use of sulfide solutions as sacrificial agents was shown in Fig. 5.1a. The hydrogen yields significantly increased from 9.39 to 14.54 $mmol.g^{-1}.h^{-1}$ when accelerating the Pt amount from 0.5 to 1.5%. However, after the optimal point, the production yields fluctuated around 14 $mmol.g^{-1}.h^{-1}$, indicating the saturated deposition of Pt on the surface of the materials.
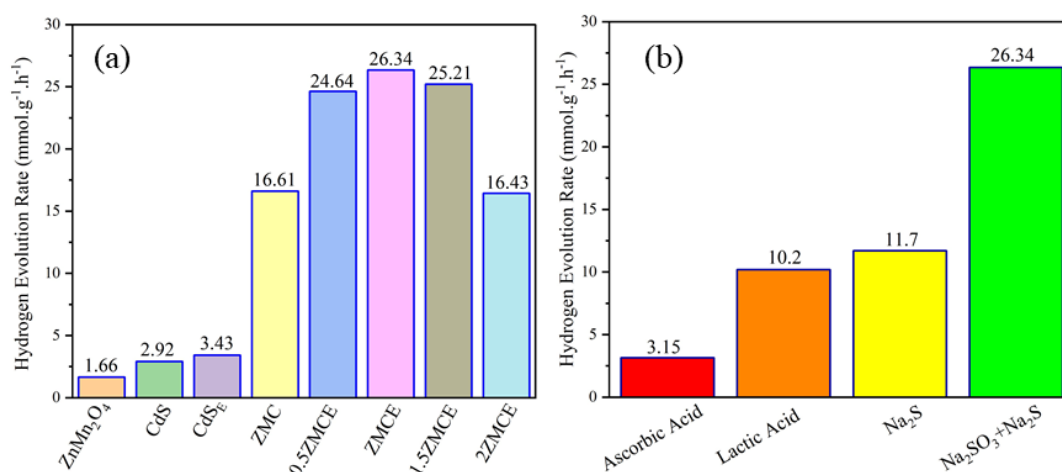
Fig. 5.2 Comparisons of photocatalytic hydrogen evolution performances: (a) Different samples; (b) Effect of different sacrificial agents on 10 mg of ZMCE

Fig. 5.1b depicted the experimental results of the use of different ZMCE amounts, ranging from 0.05 to 0.1 $mg.mL^{-1}$. It is easy to see that the hydrogen evolution rate increased from 16.77 to 26.34 $mmol.g^{-1}.h^{-1}$ with the rise of the photocatalyst's dosage, while the continuous growth in the quantity of ZMCE led to a strong decrease in the production rate. It is because the small dosage was not adequate to provide enough active sites for the reaction. Besides that, the excessive amount was blamed for the

shielding effects during light irradiation [68]. Fig. 5.2a demonstrates the comparisons of hydrogen production results from different samples using Na_2S and Na_2SO_3 as a sacrificial solution. It is obvious that the single photocatalysts exhibited low production efficacy in comparison to the composites. Particularly, $ZnMn_2O_4$ and CdS generated hydrogen at the rates of 1.66 and 2.92 $mmol.g^{-1}.h^{-1}$, respectively, while coated CdS with Na-EDTA can increase the result to 3.43 $mmol.g^{-1}.h^{-1}$. The better observation was recorded with the integration between CdS and $ZnMn_2O_4$. The sample (ZMC) was shown at a higher production rate compared to its single counterparts, with the figure being 16.61 $mmol.g^{-1}.h^{-1}$. Furthermore, a remarkable enhancement was observed when CdS was integrated with EDTA before forming a heterojunction. The optimal hydrogen evolution rate was at 26.34 $mmol.g^{-1}.h^{-1}$ for the sample consisting of CdS_E and $ZnMn_2O_4$, which was approximately 15.9, 9, and 7.7 times higher than that of pure $ZnMn_2O_4$, CdS, and CdS_E, respectively, in the same reaction conditions. It is inferred that EDTA can play a bridge between CdS and $ZnMn_2O_4$ to improve charge transportation between two materials [113]. Besides, the percentage of $ZnMn_2O_4$ was essential when establishing a junction. Notably, the lack of $ZnMn_2O_4$ could negatively influence forming of an active junction for activating the hydrogen generation by using the small amount of zinc manganese oxide, while the large quantity can prompt a shielding effect which reduces the materials' photo-activity.

The effect of different sacrificial molecules on the hydrogen production yield is highlighted in Fig. 5.2b. It is obvious that the material possessed the excellent photo-activity in the mixed sulfide solution where the obtained optimal rate of hydrogen evolution was mainly 8.4, 2.6, and 2.3 times higher than that of the solution comprising

of ascorbic acid (0.25M), lactic acid (10 mL), and Na_2S (0.35M), respectively. Understandably, electron donors can improve photocatalytic hydrogen evolution rate because they can consume holes to prevent charge recombination and suppress the formation of oxygen in which the reverse reaction would not occur. Besides that, the photodecomposition of organic molecules also contributes to producing hydrogen, leading to the improvement in the production efficacy [125]. Additionally, hole scavengers also were associated with the phase transformations of the materials during light irradiation, depending on inorganic or organic agents [126].

To study the photostability of ZMCE, the reactions were run for 18 h with the addition of the same amount of sacrificial solutions after each 3 h. As can be seen in Fig. 5.3, the hydrogen production when using the mixed sulfide solution is greater than that of its counterpart, lactic acid, for almost six cycles. After each cycle, the generated hydrogen obviously increased due to two reasons. Firstly, the longer irradiation time could have a positive effect on the formation of Pt, resulting in the enhancement in photo-hydrogen production. Secondly, the increase in the concentration of sacrificial agents would also contribute to producing a higher hydrogen amount on account of effectively scavenging holes. Therefore, in both basic and acidic environments, the composite showed better photoactivity, indicating the inhibition of photo-corrosion.
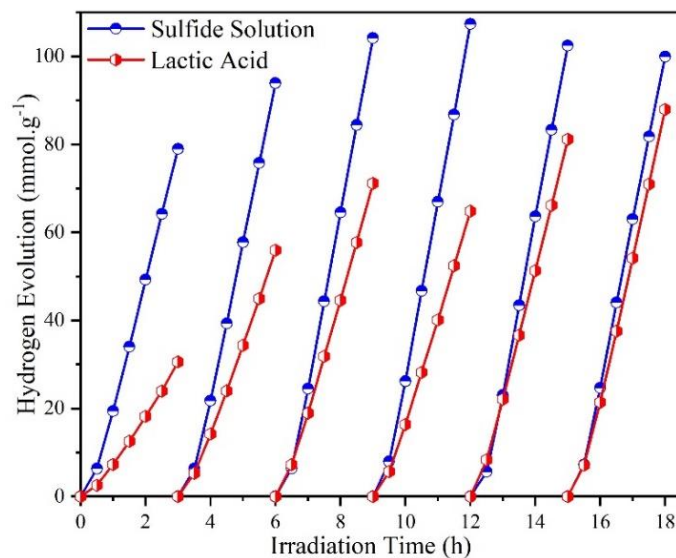
Fig. 5.3 Photostability Test for ZMCE during 18 h under sulfide and acid conditions

5.2.2 Zeta Potential Results

To understand the absorption abilities of CdS and CdS_E, zeta potential measurements were carried out in water. The zeta potential results for all samples were shown in Table 5.2. Specifically, when coating with EDTA, the surface charge of CdS_E was more negative and nearly double the value for pure CdS. In this case, EDTA molecules can make the surface more attractive to efficiently absorb cation ions such as Zn and Mn to form heterojunctions. Furthermore, the functionalized sample (CdS_E) would be more stable in water than that of pure CdS since it establishes a strong complex with CdS, presented in Fig. 5.4, which could be a good indication for successful attachments of EDTA molecules with CdS [127, 128]. $ZnMn_2O_4$ and the composite without EDTA bridges depicted the deficient dispersity in water. In addition, the composites with EDTA bridges possessing a higher amount of $ZnMn_2O_4$ also pictured the poor dispersion ability in water. These results should be greatly suitable with their zeta potential results.

52

Table 5.2 Zeta potential results of obtained photocatalysts

Sample	Zeta Potential (eV)	Electron Mobility (μmcm/Vs)	Conductivity (mS/cm)
CdS	-12.6	-0.9901	0.0429
CdS_E	-24	-1.879	0.0174
$ZnMn_2O_4$	-11.3	-0.8832	0.0525
ZMC	-14.2	-1.113	0.066
0.5ZMCE	-21.7	-1.702	0.0339
ZMCE	-21.4	-1.674	0.0699
1.5ZMCE	-18.4	-1.440	0.0613
2ZMCE	-12.7	-0.9926	0.0658
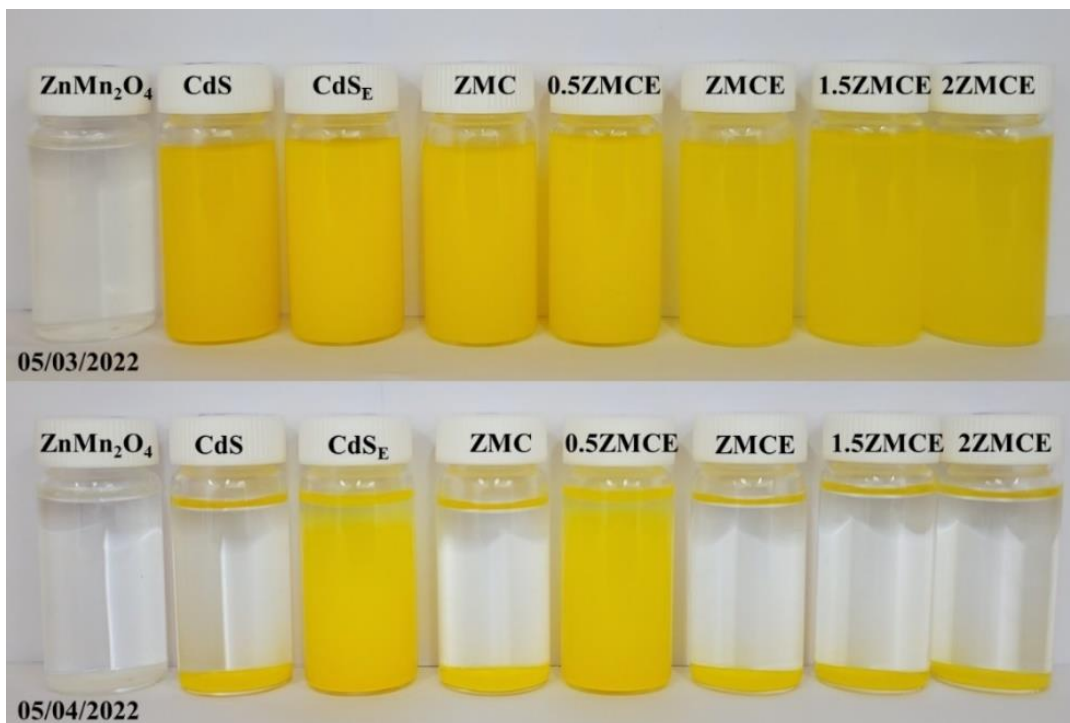
Fig. 5.4 The dispersion stability of obtained materials

5.2.3 AFM, FESEM, and EDS Analyses

AFM and FESEM analyses were undertaken to confirm the changes in the morphologies of CdS, CdS_E, $ZnMn_2O_4$, ZMC, 0.5ZMCE, ZMCE, 1.5ZMCE, 2ZMCE, and ZMCE after 3h light irradiation ($ZMCE_{used}$). As shown in Fig. 5.5a and 5.5b, while pure CdS clearly possessed the dense distribution and aggregations, the coated sample (CdS_E) shows a larger size in the AFM image with decreasing agglomeration levels. From Fig. 5.5c, $ZnMn_2O_4$ shows its large and uniform particles with a better surface area which can match well with the BET result in Table 5.3.

Further investigations of ZMC and ZMCE in Fig. 5.5d and 5.5e apparently illustrate that EDTA molecules participate in forming more heterojunctions between two materials. Without adding EDTA, CdS nanoparticles and $ZnMn_2O_4$ are separately configured on account of their low negative surface potential to attract adequate Zn^{2+} and Mn^{2+} to create $ZnMn_2O_4$. In contrast, due to the highly negative surface potential, these cation ions would effortlessly interact with CdS_E through electrostatic attraction and be absorbed on the CdS_E surfaces. It is inferred that after pouring oxalic acid into the solution, the creation of the oxalate precipitates in the bigger sizes would have happened and they were covered by CdS_E surrounding them. As a result, the formation of $ZnMn_2O_4$ during the calcination process could lead to the clear aggregations of CdS_E. A similar observation was recorded when comparing the morphologies of the composites with the various weight ratios between CdS_E and $ZnMn_2O_4$ from Fig. 5.5. The higher the weight percentage of $ZnMn_2O_4$ was, the lower aggregation of CdS_E on the surface was. Additionally, the morphologies of ZMCE after 3 h irradiation were also characterized by the clear observations of the particle's agglomerations from the AFM

54

and FESEM images in Fig. 5.5f, indicating the morphological alterations in its size. Interestingly, the above results from cycle tests show no loss in photocatalytic activities, which means the adept performances in hydrogen productions could be mainly induced by the effect of EDTA molecules on the electronic structures of the photocatalysts.
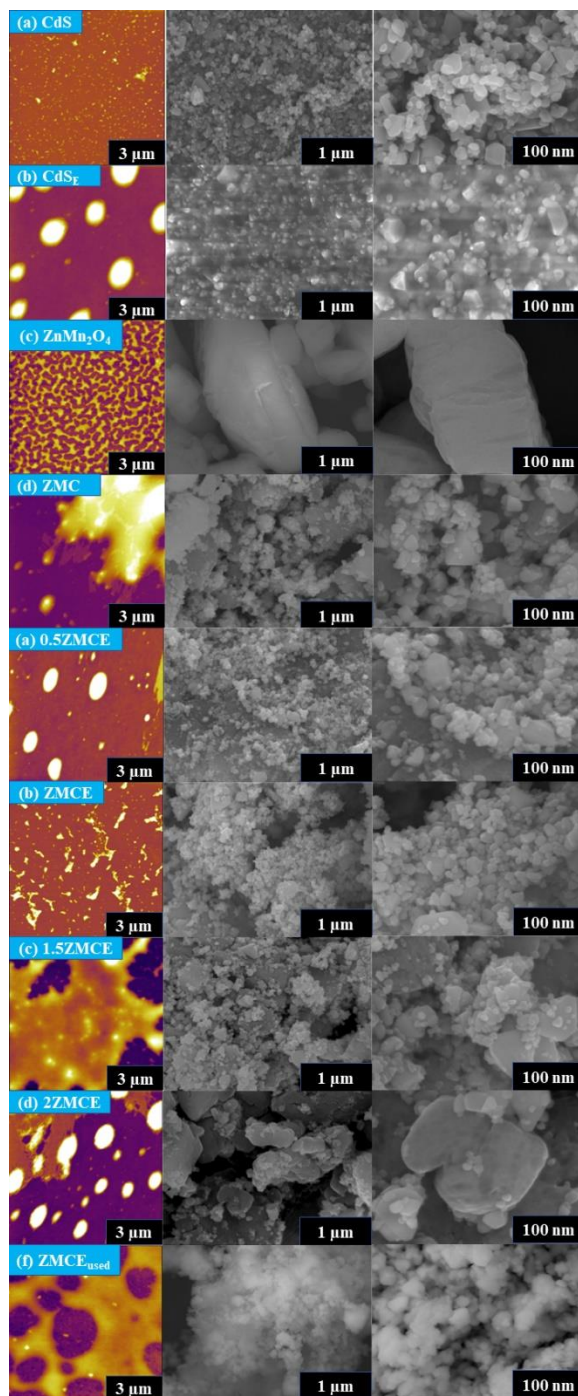
Fig. 5. 5 AFM (left) and FESEM (right) images of as-synthesized catalysts
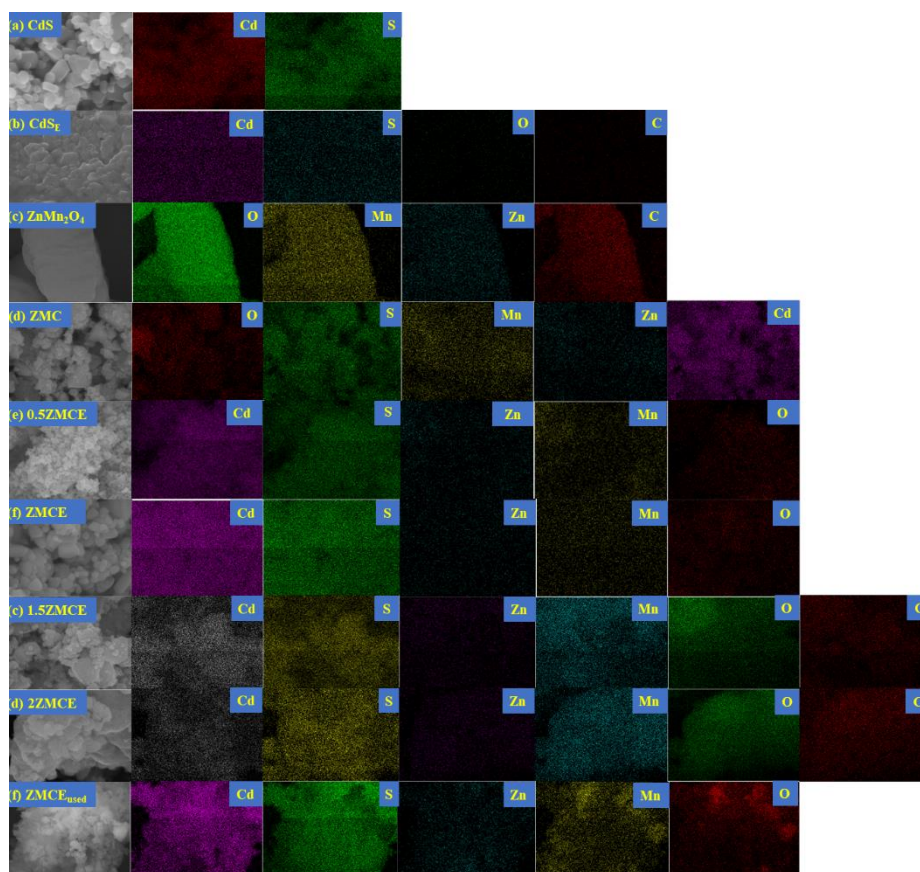
Fig. 5.6 EDS results from FESEM measurements of the obtained photocatalysts

Fig. 5.6 showed the information about elemental distributions in the materials from EDS examinations. Whereas just two elements Cd and S were recorded in Fig. 4.4a, the additional elements, O and C, were captured in the coated sample (CdS$_E$). Besides that, the EDTA molecules could help to flatten and make the distribution of Cd and S more uniform than pure CdS. Further evidence from Fig. 4.4d and 4.4f also follows this trend with more uniform CdS distributed on the entire surface. The figure for ZnMn$_2$O$_4$ demonstrated the uniform elements of Zn, Mn, O, and C on the nanoparticles. The appearance of C on this structure was mainly based on the synthetic method due to the low calcination temperature in which some functional groups of oxalate salts could not be eliminated. The elemental distribution of the remaining

samples from Fig. 5.6e to 5.6f exhibits a similar trend with the uniform formation of CdS. Eventually, the sample after light irradiation shows the same elements as the pure sample, validating the unsignificant changes in elemental compositions in which the photocatalytic activity could be maintained.

5.2.4 BET Analyses

Table 5.3 BET results of the materials

Sample	Surface Area (m²/g)	Pore Volume (cm³/g)	Pore Radius (nm)
CdS	6.695	0.238	98
CdS_E	7.023	0.134	29
$ZnMn_2O_4$	22.086	0.094	12
ZMC	16.293	0.089	2
0.5ZMCE	14.37	0.160	3
ZMCE	15.002	0.135	5
1.5ZMCE	21.452	0.106	2
2ZMCE	21.498	0.119	2

BET surface areas of CdS and CdS_E in Table 5.3 verified the efficiency of functionalized EDTA molecules into CdS to increase active sites for catalytic activities, leading to the improvement in hydrogen production results. Although $ZnMn_2O_4$ possessed the highest surface area in the synthesized materials, it is poorly active in visible light which induces the lower photo-hydrogen generation efficacy. The surface area of the composite between CdS and $ZnMn_2O_4$ shows a greater result than that of

pure CdS, increasing from 6.695 to 16.293 m^2/g for CdS and ZMC, respectively. However, the determined BET result for ZMCE was lower than that of ZMC owing to the role of EDTA molecules in which CdS nanoparticles were densely allocated on the entire surface of oxide particles. It is obvious that there was a growth in the BET surface area values of the composites with increasing in the quality of ZnMn$_2$O$_4$. The phenomenon could be seriously consistent with the results obtained from AFM and FESEM images.

5.2.5 XRD Characterizations
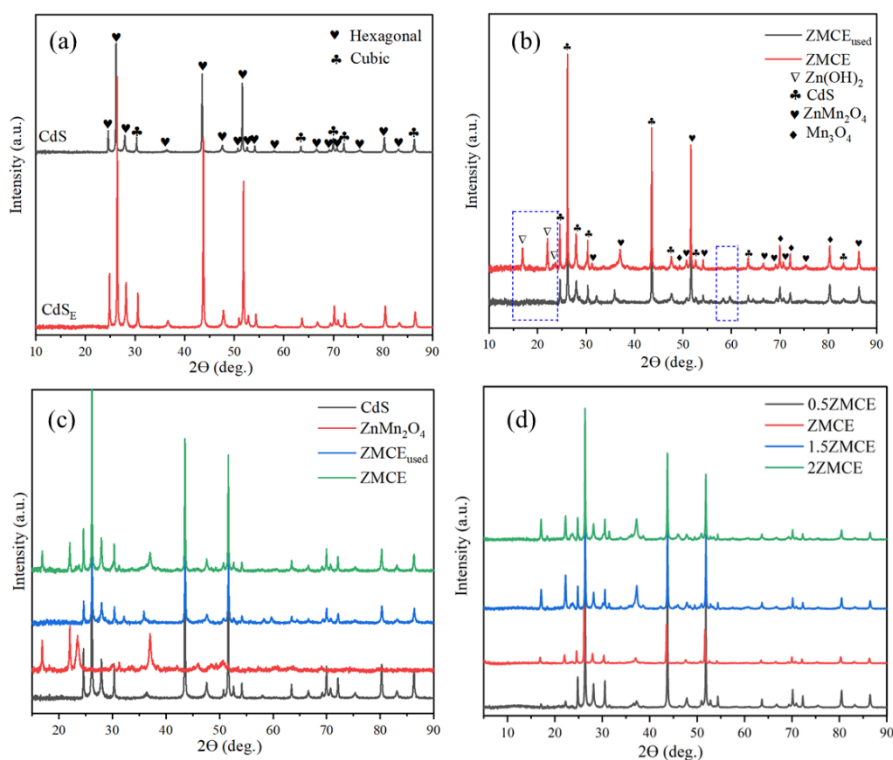
Fig. 5.7 XRD Patterns of as-prepared photocatalysts

Fig. 5.7a and 5.7b give information about the XRD patterns of CdS, CdS$_E$, ZMCE, and ZMCE after light irradiation (ZMCE$_{used}$). The XRD patterns of all samples were reported in Fig. 5.7 with similar positions of their peaks. From Fig. 5.7a, there

58

were two phases of CdS in the sample, including cubic and hexagonal structures. While the two theta degree peaks located at 24.6° (100), 26.14° (002), 27.92° (101), 36.38° (102), 43.54° (110), 47.56° (103), 50.74° (200), 51.64° (112), 52.62° (201), 54.16° (004), 58.08° (202) , 66.42° (203), 69.36° (210), 70.76° (211), 75.34° (212), 80.14° (300), and 83.02° (213) belonged to the hexagonal crystalline structure of CdS, the other peaks at 30.38° (200), 63.62° (400), 70.08° (331), 72.22° (420), and 86.16° (511) were associated with CdS cubic system. These peaks accurately matched with JCPDS Card No. 01-083-5246 for hexagonal crystal and JCPDS Card No. 00-010-0454 for its counterpart. In addition, when coating CdS with EDTA, the intensity of CdS_E in the XRD result apparently increased, suggesting better crystallization in CdS structures. From Fig. 5.7b, apart from several peaks belonging to the CdS structures, the remaining peaks show the composites including $Zn(OH)_2$, $ZnMn_2O_4$, and Mn_3O_4. Particularly, three peaks situated at 16.98° (001), as well as 22.06° (110) and 23.88° (101) were attributed to the β-$Zn(OH)_2$ (JCPDS Card No. 20-1435) and ϵ-$Zn(OH)_2$ (JCPDS Card No. 38-0385), respectively [126, 129, 130]. However, no observations of these peaks in $ZMCE_{used}$ indicate the transformation of $Zn(OH)_2$ into ZnO based on the dissolution of $Zn(OH)_2$ [131]. Whereas the recorded peaks at 31.28° (101), 37.02° (202), 50.78° (204), 51.64° (105), 66.6° (323), 69.22° (206), 70.74° (305), 86.52° (424) were related to the tetragonal structure of $ZnMn_2O_4$ (JCPDS Card No. 00-024-1133), four additional peaks for tetragonal Mn_3O_4 were also observed, including 49.32° (204), 69.96° (305), 72.08° (332), and 80.26° (316) (JCPDS Card No. 00-024-0734). Two new peaks appeared in the $ZMCE_{used}$ pattern at 58.38° (321) and 59.72° (224) were marked for tetragonal Mn_3O_4 with the same standard pattern, recommending the effect of light on

transforming the crystal structure of the prepared materials. Although the patterns for ZMCE and ZMCE$_{used}$ involved some small changes in the structures, these are almost identical to each other which can validate the photostability of the heterojunction structures.

5.2.6 FTIR Results

FTIR spectra of different samples were performed to investigate the functional groups of the materials. In Fig. 5.8a, the FTIR spectrum of CdS$_E$ reflected some organic functional groups in comparison with the spectra for pure CdS and Na-EDTA. For example, the strong peak from CdS$_E$ spectrum at about 1614 cm^{-1} corresponds to the C=C vibrations of the asymmetrical COO-, indicating that some EDTA molecules successfully functionalized CdS [113]. All FTIR spectra for the materials could be seen in Fig. 5.8 and the locations of their peaks were similar to each other, indicating the similar structures of the materials. Noticeably, the singlet and doublet peaks at around 3400 and 1350 cm^{-1} in Fig. 6d disappeared after 3 h visible light irradiation because of the photo-degradation of organic functional groups to form oxide structures. These strong peaks were assigned to O-H and O-C-O bonds from zinc and manganese oxalate [132]. Furthermore, three small peaks located at approximately 441, 495, and 540 cm^{-1} could be ascribed to the vibrations of Mn-O and Zn-O in ZnMn$_2$O$_4$ spinel oxides [133].
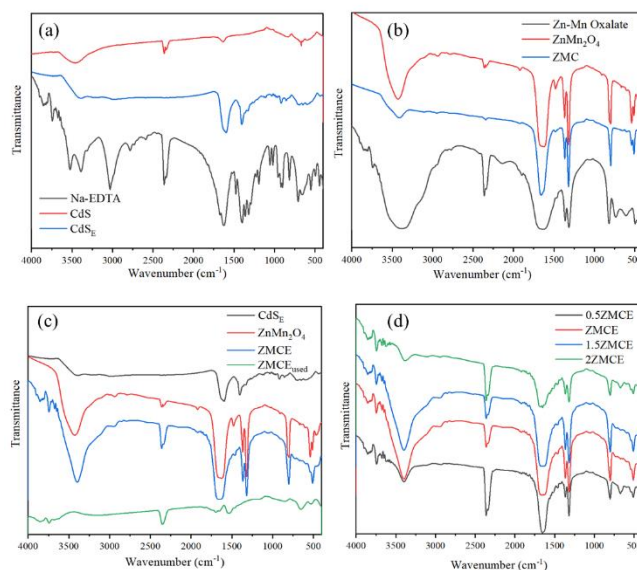
Fig. 5.8 FTIR spectra of as-synthesized photocatalysts

5.2.7 XPS Analyses

XPS measurements were carried out to determine the chemical compositions and elemental states of the materials. In Fig. 5.9a, the XPS survey spectra of ZMCE and ZMCE$_{used}$ show the similarity in elemental compositions between the two samples, informing the stability of as-prepared photocatalysts during the exposure to visible light. From the spectra, there were 6 similar core elements in both samples, including Cd 5.9d, Mn 2p, Zn 2p, O 1s, C 1s, and S 2p. For ZMCE$_{used}$, there was one additional core element Pt. The deconvolution peaks for Cd 3d from Fig. 5.9b consisted of 404.9, as well as 411.4 and 412.5 eV corresponding to Cd $3d_{5/2}$, and Cd $3d_{3/2}$, respectively. The calculated spin-splitting level was approximately 7.6 eV, suggesting the Cd^{2+} state [134, 135, 136]. Two peaks located at 641.9 and 652.2 eV in Fig. 5.9c were individually assigned to Mn $2p_{1/2}$ and Mn $2p_{3/2}$, with the difference in the spin-orbit energy level around 10.3 eV indicating the replacement of Mn for O in the spinel oxide [137]. However, the satellite peak at 652.3 eV recommended the state of Mn^{4+} in the sample.

Additionally, the deconvolution peaks at 1022.1 and 1045.3 eV in Fig. 5.9d were compatible with Zn $2p_{3/2}$ and Zn $2p_{1/2}$ with the energy spacing being 23.2 eV, revealing the existence of the Zn^{+2} state in $ZnMn_2O_4$ crystals [138, 139]. Furthermore, the fitting peaks at 284.6, 286.1, 288.1, and 288.5 eV from C 1s in Fig. 5.9e demonstrate the presence of EDTA molecules in the materials since these peaks were sequentially attributed to C-C, -N-C-(C), N-C=N or -N-C-(C), and O-C=O [113, 140]. Besides, the scanned XPS spectrum of O 1s of ZMCE in Fig. 5.9f depicts that the sample possessed two types of oxygen bonding states, including lattice oxygen of the oxides and hydroxyl group or surface-absorbed oxygen, which in turn matched with the peaks situated at 531.2 and 532 eV [120]. Fig. 5.9g shows two convoluted peaks at 160.8 and 161.8 eV representing typical signals for S^{2-} ions inside the sample with the difference between two characteristic energies being around 1 eV [141]. The chemical state of Pt 5.9f in the sample after 3 h irradiation was also examined in Fig. 5.9h. There were two oxidation states of Pt^0 and Pt^{2+} in the sample. In previous reports, the presence of Pt^{2+} was also responsible for the increase in hydrogen production because of the suppression of hydrogen oxidation reaction [142]. The XPS results validated the successful attachment of $ZnMn_2O_4$ into CdS via EDTA bridges to enhance charge transportation, and the introduction of different Pt species through the photodecomposition process into the material effectively promoted the hydrogen production rate.
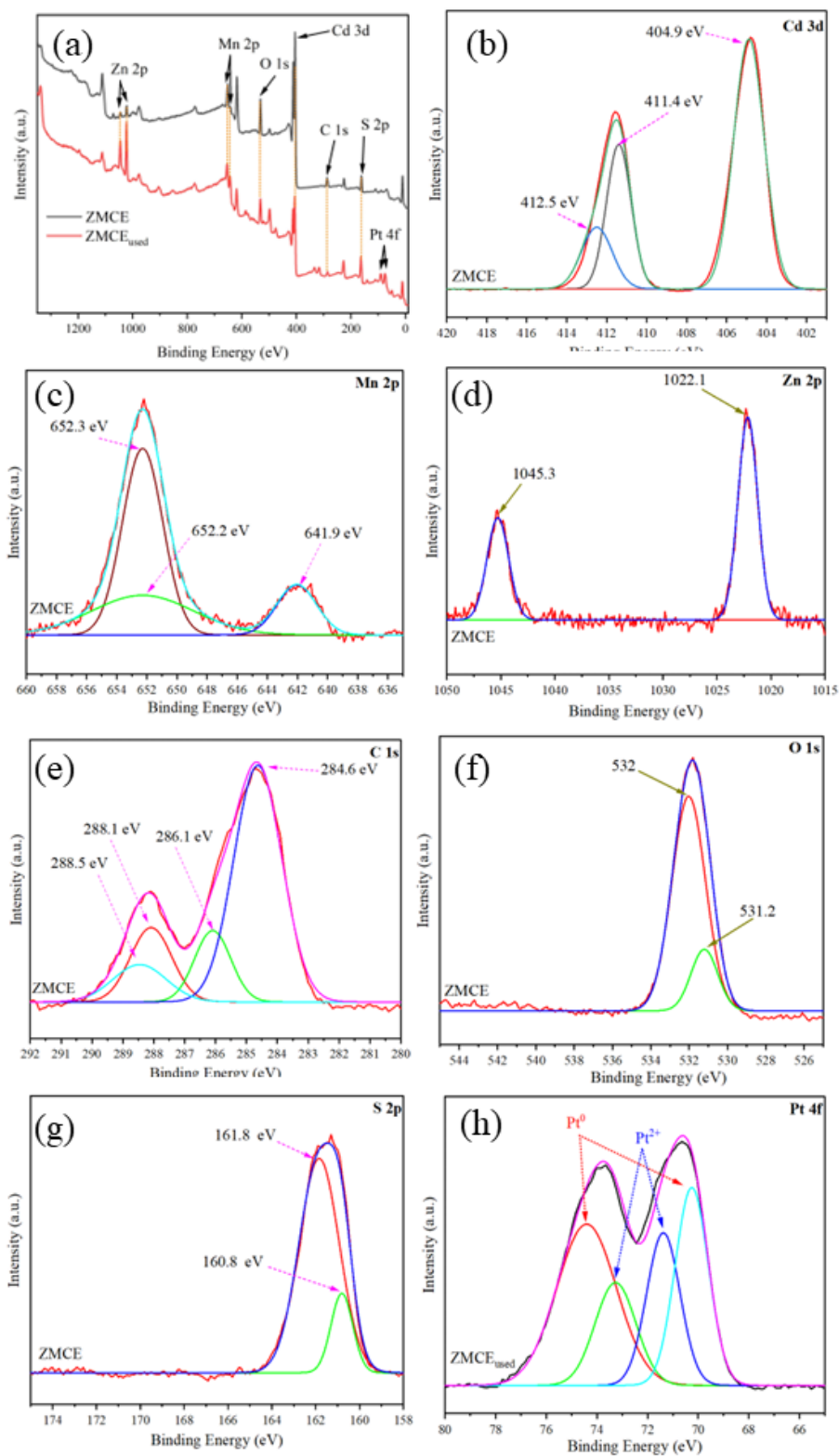
Fig. 5.9 XPS survey spectra of ZMCE and ZMCE_{used} (a); Cd 3d (b), Mn 2p (c), Zn 2p (d), C 1s (e), O 1s (f), and S 2p (g) of ZMCE; Pt 4f (h) of ZMCE_{used}

5.2.8 UV-Vis-DRS Results

Fig. 5.10a displays the UV-Vis-DRS absorption spectra of the synthesized materials. It is easy to see that $ZnMn_2O_4$ possesses absorption from around 250 to 450 nm, which was mostly active in the UV region. Besides, CdS shows the range from 450 to 550 nm in contrast with the broader response in visible light of CdS_E sample from 450 to 650 nm, proving the positive effect of attaching EDTA on CdS molecules to increase visible light absorption. Moreover, the composite without EDTA attachments also demonstrates a smaller visible light absorption region in comparison with the composite including EDTA which these results were suitable from the literature [143]. The entire spectra of all obtained samples were shown in Fig. 5.10a which possessed similar results. To understand more insights into the light absorption efficiency from the samples, the bandgap energies (E_g) were plotted by using the Kubelka Munk equation, represented in Fig. 5.10b, 5.10c, and 5.10d. Fig. 5.10c illustrates the bandgap energy of $ZnMn_2O_4$ with the determined value at 3.63 eV, which was larger than the reporting value of around 2 eV [110, 144]. This phenomenon could be explained by the interaction of some impurities from Mn_3O_4, $Zn(OH)_2$, and functional groups on $ZnMn_2O_4$ when calcinating at a low temperature. On the other side, CdS_E possessed lower bandgap energy than pure CdS with the figure being 2.26 and 2.27 eV, respectively, proving the role of EDTA in the coated sample to decrease the bandgap energy and effectively absorb more visible light. The energies for ZMC and ZMCE also illustrate a similar trend with these values at 2.29 and 2.28 eV, individually. Therefore, these results could validate the enhancement in visible light absorption for

64

heterojunction photocatalysts in which the bandgap energies would be lowered to boost the photocatalytic activities of the materials.
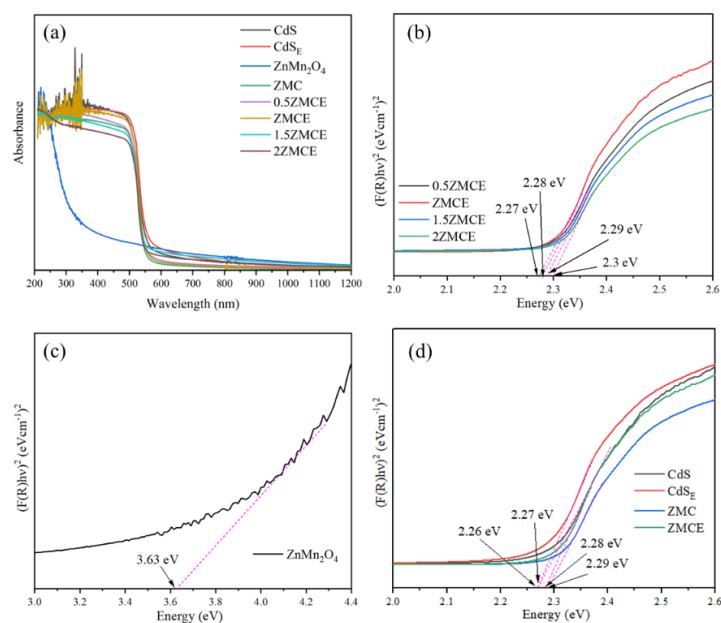
Fig. 5.10 (a) The UV-Vis DRS absorbance spectra of the materials; (b)-(d) The optical band gap energies of obtained samples through a Kubelka-Munk model

5.2.9 XPS Valance Band Results
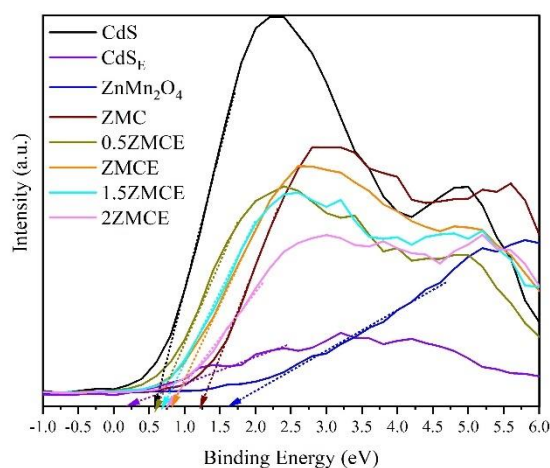
Fig. 5.11 The valance band energy from XPS valance spectra

It has been stated that the UV-Vis-DRS spectra could not completely determine the efficiency of photocatalysts because the catalytic behaviors would be reliant on their conduction band (CB) and valance band (VB) positions in the redox potential scale, leading to the requirement for more characterizations [110]. Theoretically, the VB energy (E_V) and the CB energy (E_C) could be calculated based on Equation (5.1) as follows:

$$E_c = E_v - E_g \tag{5.1}$$

Fig. 5.11 evinced the VB positions of the obtained materials from XPS valance band measurements. Obviously, the valance energies of CdS, CdS$_E$, ZnMn$_2$O$_4$, ZMC, and ZMCE were sequentially at 0.58, 0.16, 1.64, 1.23, and 0.69 eV. It is transparent that EDTA functionalized CdS played a vital role in decreasing the valance energy of the pure sample with the different level being 0.42 eV, in which the conduction band energy of CdS was more negative, contributing to the higher efficiency in water reduction process. A similar phenomenon was observed in the composites with a significant decrease of ZnMn$_2$O$_4$ from 1.64 eV to 1.23 eV for ZMC and 0.69 eV for ZMCE which can demonstrate the importance of EDTA bridges to enhance photocatalyst's electronic structures for hydrogen production. Based on Equation (5.1), the electronic positions of obtained samples are plotted in Fig. 5.12 with the entire electronic data in Table 5.4.
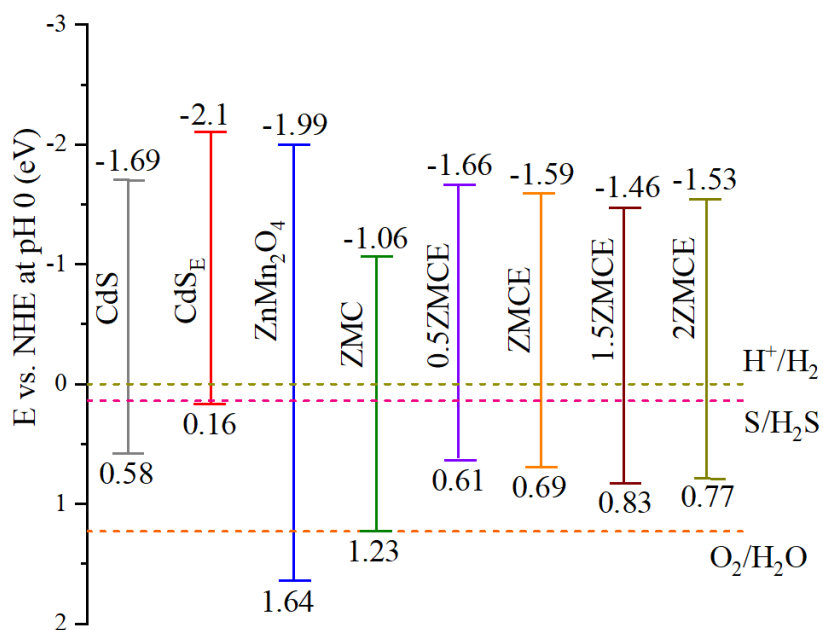
Fig. 5.12 Band structure of as-synthesized photocatalysts

Table 5.4 Electronic properties of as-synthesized materials

Sample	Bandgap Energy (eV)	Valance Band Energy (eV)	Conduction Band Energy (eV)
CdS	2.27	0.58	-1.69
CdS$_E$	2.26	0.16	-2.1
ZnMn$_2$O$_4$	3.63	1.64	-1.99
ZMC	2.29	1.23	-1.06
0.5ZMCE	2.28	0.61	-1.67
ZMCE	2.27	0.69	-1.58
1.5ZMCE	2.29	0.83	-1.46
2ZMCE	2.3	0.77	-1.53

5.2.10 PL and TRPL Results
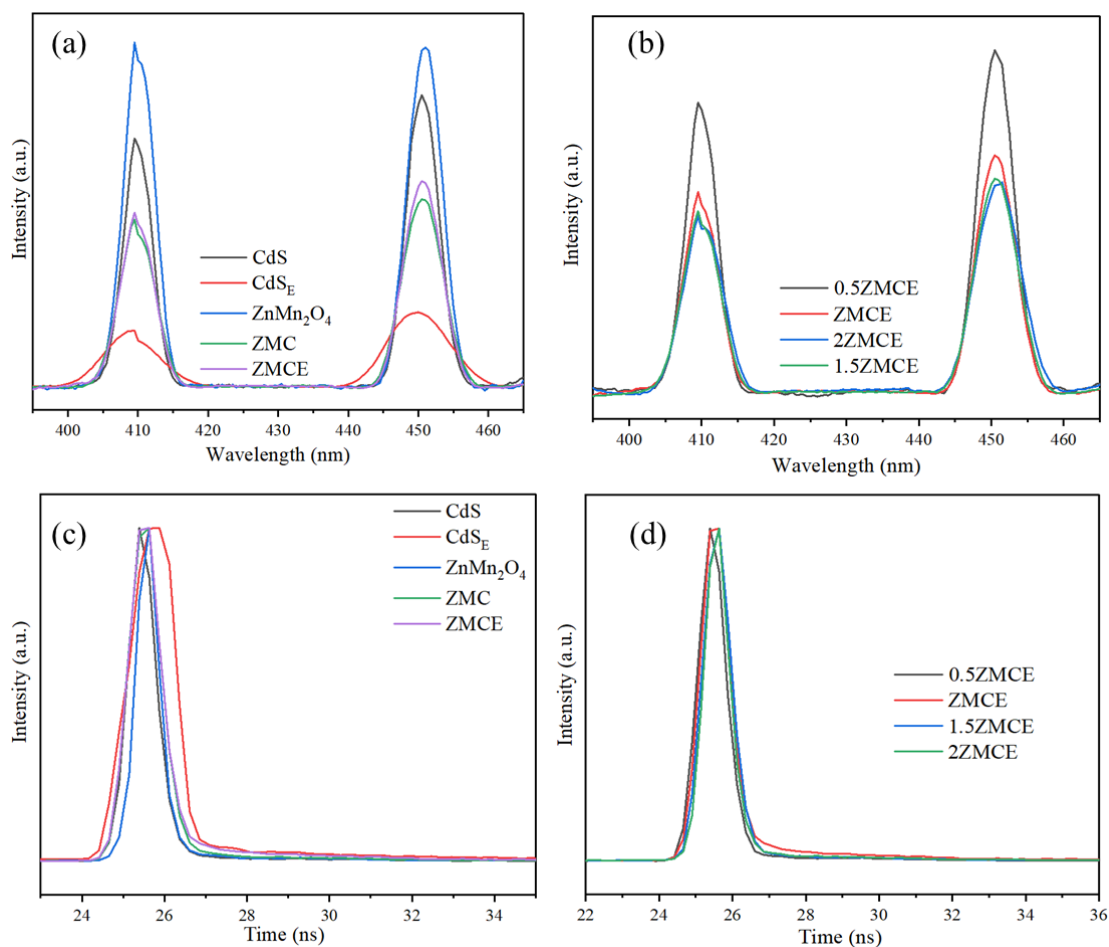
Fig. 5.13 (a)-(b) Steady-state PL spectra; (c)-(d)Time-resolved PL spectra of as-prepared photocatalysts

An excitation wavelength at 350 nm was used for PL and TRPL measurements to examine the charge separation efficiency in the materials. A higher PL intensity could be considered as a higher charge recombination in the photocatalysts [110]. As illustrated in Fig. 5.13a and 5.13b, the steady-state PL spectra of all samples have dual peaks at around 440 and 450 nm. The result for CdS showed a notably significant recombination rate of charge carriers that were on the contrary with CdS_E, indicating the promotion of charge transfers when coating with EDTA. The additional PL

information of the composites followed a similar trend in which the cooperation between two materials forming heterostructure photocatalysts could enhance charge transportations, proved by lower PL intensities. Further investigations of TRPL measurements could confirm the results. The spectra were examined at the same excitation wavelength (350 nm). Fig. 5.13c and 5.13d expressed the emission decay profiles of the obtained materials. The whole results could be found in Table 5.5 in which the radiative lifetimes were calculated by the tri-exponential fitting model. From Table 5.5, the calculated average lifetimes of CdS, CdS_E, $ZnMn_2O_4$, ZMC, and ZMCE were in turn at 1.32, 1.48, 0.77, 1.68, and 4.49 ns. The results could match well with steady-state PL spectra, which EDTA could help to prolong the lifetime of photoexcited charge carriers in comparison between CdS and CdS_E. While $ZnMn_2O_4$ performed the lowest lifetimes, the introduction of CdS or CdS_E to form the heterojunction structures strongly ameliorated the results. The lifetimes of the composites increased 2.2 and 5.8 folds compared to that of $ZnMn_2O_4$, resulting in a superior enhancement in hydrogen production rate. In consequence, the PL and TRPL results could be strong evidence of the role of EDTA and the heterojunction structures to advance the electron-hole pair separation process and retard charge recombination.

Table 5.5 Time-resolved PL fitted results

Sample	t_1 (ns)	A_1 (%)	t_2 (ns)	A_2 (%)	t_3 (ns)	A_3 (%)	t_{ave} (ns)
CdS	0.21	65.87	3.46	34.13	-	-	1.32
CdS_E	0.18	64.2	3.80	35.8	-	-	1.48

ZnMn$_2$O$_4$	0.22	84.1	3.69	15.9	-	-	0.77
ZMC	0.28	81.37	3.52	16.44	40	2.19	1.68
0.5ZMCE	0.2	67	3.18	26.23	52.77	6.77	4.54
ZMCE	0.29	66.54	3.56	26.77	50	6.68	4.49
1.5ZMCE	0.28	84.36	3.61	12.04	50	3.6	2.47
2ZMCE	0.26	80.64	3.37	16.3	50	3.06	2.29

5.2.11 EIS Results

EIS measurements were frequently scrutinized to get a better understanding of the photo-induced charge separation process for photocatalytic materials [145]. Fig. 5.14a and 5.14b proclaim the Nyquist plots of synthesized materials. It has been asserted that the smaller an arc radius of the material was, the better the electron-hole pair separation rate was because of the low electron transfer resistance, supporting the photocatalytic process [144]. From the EIS results, ZnMn$_2$O$_4$ revealed the largest arc radius, whereas CdS arc radius ranked second, manifesting the low photoactivity due to its high resistance. However, when attaching CdS with EDTA molecules, a clear decrease was observed. This phenomenon also occurred for the composites with EDTA molecules and without EDTA molecules. These EIS outcomes could be in great accordance with the PL and TRPL to reinforce the role of EDTA bridges to lengthen electron-hole separation lifetimes and reduce electron transfer resistance.
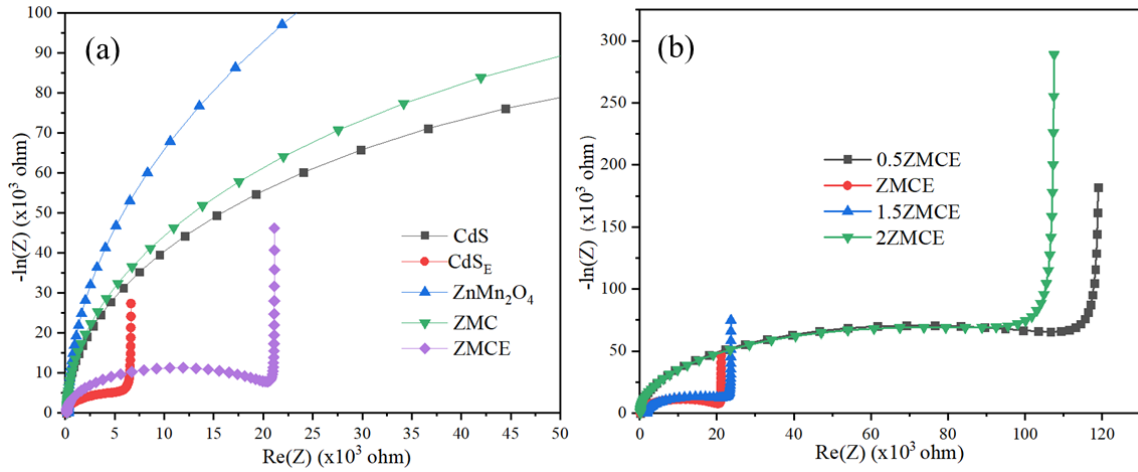
Fig. 5.14 EIS Nyquist plots of the obtained samples

5.2.12 Photocatalytic Mechanism

To get insights into the flow of electrons in the photocatalysts, UPS was exploited to determine the work function values that were shown in Fig. 5.13. The work function was evaluated based on Equation (5.2):

$$W = hv - E_{cutoff} \tag{5.2}$$

where hv and E_{cutoff} are the photon energy for He I, 21.2 (eV), and the binding energy (eV) from the UPS spectra, respectively.
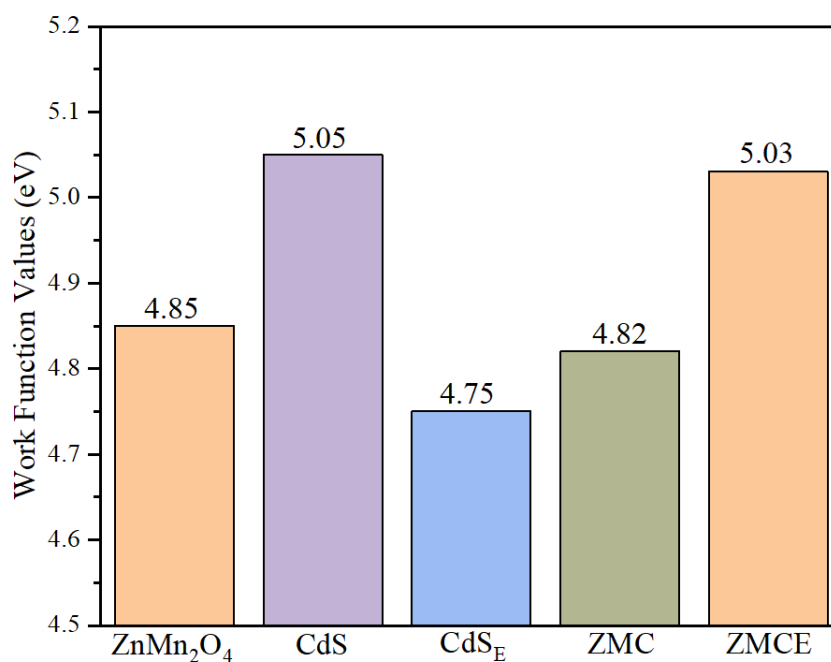
Fig. 5.15 The calculated work function from UPS spectra of materials

It has been averred that electron would move from the semiconductor with the low work function value to the higher work function semiconductor to induce the internal electronic fields, facilitating or averting further transportations of photo-induced electrons in heterojunction photocatalysts during light irradiation [110]. The work function values of $ZnMn_2O_4$, CdS, and CdS_E were 4.85, 5.05, and 4.75 eV, Fig. 5.15, proving the excited electrons will move from $ZnMn_2O_4$ to CdS for ZMC and from CdS_E to $ZnMn_2O_4$ for ZMCE. Based on these results, the photocatalytic hydrogen mechanism was proposed in Fig. 5.16. The band structures of $ZnMn_2O_4$, CdS, and CdS_E before contact with the differences in the fermi energy level (E_F) of two semiconductors were represented. After establishing a heterojunction, the alignment of E_F between two semiconductors occurred. Upon the light irradiation, the excited electrons and holes will appear in both materials at their VB and CB. From the aforementioned statement, excited electrons will flow from CB of $ZnMn_2O_4$ to CB of CdS or from CB of CdS_E to

CB of $ZnMn_2O_4$ before reaching into Pt nanoparticles to reduce water into hydrogen. In the flow of excited holes, it would go in the same direction from VB of $ZnMn_2O_4$ to VB of CdS and CdS_E because of the type I and type II heterojunction photocatalysts [110]. The other part was a Schottky junction of Pt and the composite, which would increase the electron and hole transportations as well as diminish charge recombination rate. With the formation of Pt on the surface of the heterojunctions, there were several effects simultaneously occurring to promote the reduction of water [124]. Therefore, the multiple charge transfer pathways, the localized surface plasmonic resonance, and electron sink effects from these formed junctions and Pt nanoparticles could be mainly responsible for an effective photo-induced charge transfer and eventually enhance photocatalytic hydrogen generation performance.
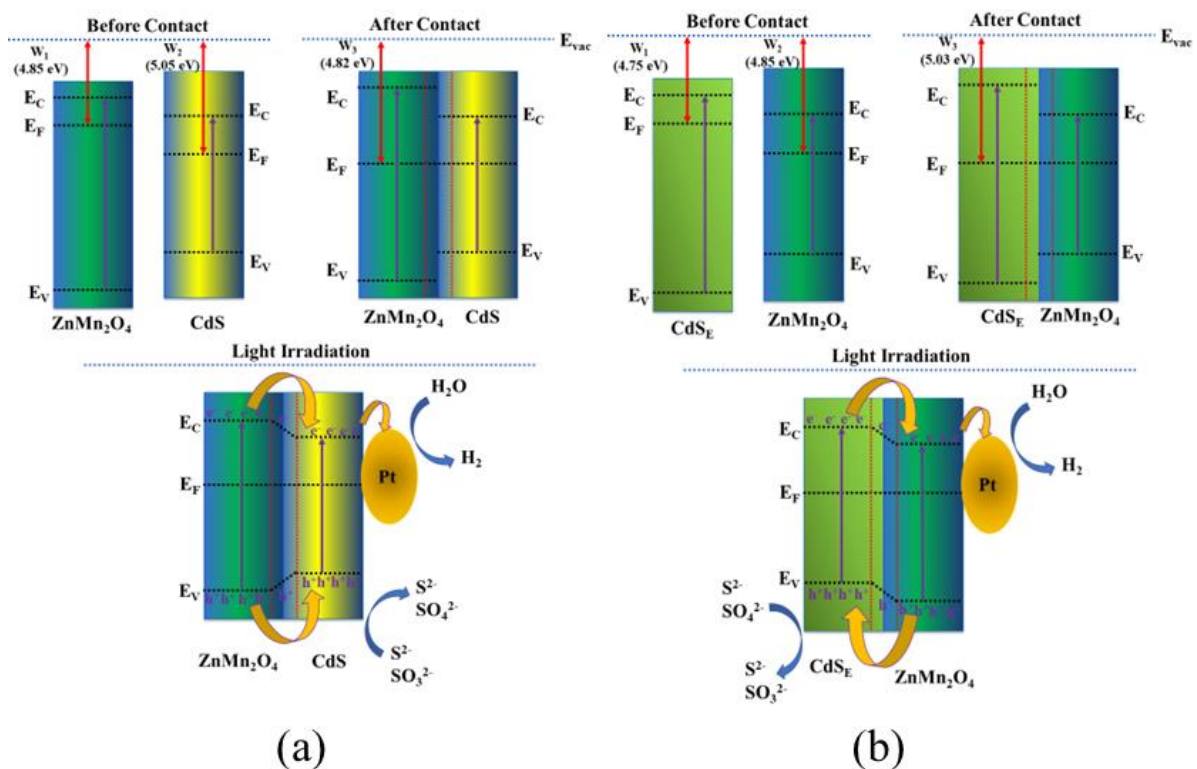
Fig. 5.16 The possible photocatalytic mechanism of ZMC (a) and ZMCE (b)

5.3 Conclusion

In this study, the fabrication of $CdS/ZnMn_2O_4$ via the EDTA bridges was reported. EDTA molecules play a pivotal role in the obtained materials to stick more CdS on the surface of $ZnMn_2O_4$ to increase photocatalytic activities leading to the enhancement in hydrogen production efficiency. Moreover, the electronic structure of the catalysts was significantly altered in the presence of EDTA molecules. The bridges also improve charge transportations and retard the recombination of the electron-hole pair that were responsible for the superior increment in hydrogen evolution rate. This research could validate the efficacy of heterojunction photocatalysts for energy applications and pave the way for further investigations into light-harvesting materials.

CHAPTER 6: CONCLUSIONS AND RECOMMENDATIONS

In summary, the photocatalytic hydrogen evolution reaction was mostly based on the electronic structures and surface properties of the materials. This research is fundamental to the idea of modified electronic structures of photocatalysts to improve their efficiency. Heterojunction photocatalysts with various mechanisms are useful for practical applications in which the flow of electrons and the electronic properties of materials could be easy to control and obtain better results.

For p-n heterojunction photocatalysts, the synthesis of Cu-Cu$_2$O/ZnO/mRGO showed their efficiency. The one-pot solvothermal technique was applied to synthesize the materials. It has clearly presented that the simultaneous effects between Cu-Cu$_2$O and mRGO contributed to significant enhancements in narrowing the bandgap energy of ZnO in which the light absorption could be more effective. Besides that, the presence of Cu could be responsible for boosting the hydrogen generation amount due to the electron donor properties, providing a better way to improve the photocatalytic activities of the materials and tackle the drawback of rapid recombination rate.

For type II heterojunction photocatalysts, the fabrication of ZnMn$_2$O$_4$/CdS via EDTA bridges could validate their potential applications. In the study, EDTA molecules clearly demonstrate their role in the composites. These molecules were efficient to decorate more CdS into the free surface of ZnMn$_2$O$_4$ which increased charge transfers and prevented charge carriers' recombination. Moreover, the sample with EDTA illustrates the small art radius of resistance under light irradiation, indicating a good photocatalyst with higher hydrogen efficiency.

For future work, there are several remaining types of heterojunctions photocatalysts that could support widening the studies. The Z-scheme and S-scheme were potential for ZnO-based heterostructures in which the entire picture could be drawn. The other aspect that should be focused on is the surface properties of the photocatalysts to improve the catalytic activities.

REFERENCES

[1] Q. Wang & K. Domen, Particulate Photocatalysts for Light-Driven Water Splitting: Mechanisms, Challenges, and Design Strategies, Chem. Rev. 120 (2020), 919-985.

[2] Y. Goto, T. Hisatomi, Q. Wang, T. Higashi, K. Ishikiriyama, T. Maeda, Y. Sakata, S. Okunaka, H. Tokudome, M. Katayama, S. Akiyama, H. Nishiyama, Y. Inoue, T. Takewaki, T. Setoyama, T. Minegishi, T. Takata, T. Yamada, K. Domen, A Particulate Photocatalyst Water-Splitting Panel for Large-Scale Solar Hydrogen Generation, Joule 2 (2018), 509-520.

[3] Z. Zhang, X. Zhou, J. Hu, T. Zhang, S. Zhu, Q. Zhang, Photo-bioreactor structure and light-heat-mass transfer properties in photo-fermentative bio hydrogen production system: A mini review, Int. J. Hydrog. Energy 42 (2017) 12143-12152.

[4] A. A. Basheer, I. Ali, Water photo splitting for green hydrogen energy by green nanoparticles, Int. J. Hydrog. Energy 44 (2019) 11564-11573.

[5] I. Staffell, D. Scamman, A. V. Abad, P. Balcombe, P. E. Dodds, P. Ekins, N. Shah and K. R. Ward, The role of hydrogen and fuel cells in the global energy system, Energy Environ. Sci. 12 (2019) 463-491.

[6] A. Bhirud, N. Chaudhari, L. Nikam, R. Sonawane, K. Patil, J. Baeg, B. Kale, Surfactant tunable hierarchical nanostructures of $CdIn_2S_4$ and their photohydrogen production under solar light, Int. J. Hydrog. Energy 36 (2011) 11628-11639.

[7] X. Zhang, Y. Zhou, D. Wu, R. Zhang, H. Liu, C. Dong, J. Yang, S. Kulinich, X. Du, ZnO nanosheets with atomically thin ZnS overlayer for photocatalytic water splitting, J. Mater. Chem. A 6 (2018) 9057-9063.

[8] J. Pan, S. Shen, W. Zhou, J. Tang, H. Ding, J. Wang, L. Chen, C. Au, S. Yin, Recent Progress in Photocatalytic Hydrogen Evolution, Acta Phys. ChimChem. Sin. 36 (2020) 1905068.

[9] B. Wang, D. Zhao, M. Song, P. Guo, S. Shen, D. Li, S. Yang, enhanced photocatalytic hydrogen evolution by partially replaced corner-site C atom with P in g-C_3N_4, Appl. Catal. B 244 (2019) 486-493.

[10] C. Rodwihok, K. Charoensri, D. Wongratanaphisan, W. M. Choi, S. H. Hur, H. J. Park, J. S. Chung, Improved photocatalytic activity of surface charge functionalized ZnO nanoparticles using aniline, J. Mater. Sci. Technol. 76 (2021) 1-10.

[11] A. Kushwaha, M. Aslam, ZnS shielded ZnO nanowire photoanodes for efficient water splitting, Electrochem. Acta 130 (2014) 222-231.

[12] Q. Chen, R. Tong, X. Chen, Y. Xue, Z. Xie, Q. Kuang, L. Zheng, Ultrafine ZnO quantum dots modified TiO_2 composite photocatalysts: the role of quantum size effect in heterojunction enhanced photocatalytic hydrogen evolution, Catal. Sci. Technol. 8 (2018) 1296-1303.

[13] Y. T. Prabhu, Y. T. Prabhu, M. V. Shankar, B. Sreedhar, U. Pal, Facile hydrothermal synthesis of CuO@ZnO heterojunction nanostructures for enhanced photocatalytic hydrogen evolution, New J. Chem. 43 (2019) 6794-6805.

[14] P. Gomathisankar, P. Gomathisankar, P. Gomathisankar, P. Gomathisankar, K. Funasaka, S. Kaneco, Photocatalytic Hydrogen Production from Aqueous Na_2S + Na_2SO_3 Solution with B-Doped ZnO, ACS Sustainable Chem. Eng. 1 (2013) 982-988.

[15] D. Commandeur, G. Brown, E. Hills, J. Spencer, Q. Chen, Defect-Rich ZnO Nanorod Arrays for Efficient Solar Water Splitting, ACS Appl. Nano Mater. 2 (2019) 1570-1578.

[16] D. Commandeur, G. Brown, P. McNulty, C. Dadswell, J. Spencer, Q. Chen, Yttrium-Doped ZnO Nanorod Arrays for Increased Charge Mobility and Carrier Density for Enhanced Solar Water Splitting, J. Phys. Chem C 123 (2019) 18187-18197.

[17] I. Ahmad, M. S. Akhtar, E. Ahmed, M. Ahmad, V. Keller, W. Q. Khan, N.R. Khalid, Rare earth co-doped ZnO photocatalysts: Solution combustion synthesis and environmental applications, Sep. Purif. Technol. 237 (2020) 116328.

[18] D. Hong, G. Cao, X. Zhang, J. Qu, Y. Deng, H. Liang, J. Tang, Construction of a Pt-modified chestnut-shell-like ZnO photocatalysts for high-efficiency photochemical water splitting, Electrochem. Acta 283 (2018) 959-969.

[19] M. Hsu, C. Chang, H. Weng, Efficient H2 Production Using Ag_2S-Coupled ZnO@ZnS Core−Shell Nanorods Decorated Metal Wire Mesh as an Immobilized Hierarchical Photocatalyst, ACS Sustainable Chem. Eng. 4 (2016) 1381-1391.

[20] C. Tan, A. K. S. S. Zin, Z. Chen, C. H. Liow, H. T. Phan, H. R. Tan, Q. Xu, and G. W. Ho, Inverse Stellation of CuAu-ZnO Multimetallic Semiconductor Nanostartube for Plasmon Enhanced Photocatalysis, ACS Nano 12 (2018) 4512-4520.

[21] W. Y. Lim, H. Wu, Y. Lim, and G. W. Ho, Facilitating charge transfer of ZnMoS4/CuS p-n heterojunction through ZnO intercalation for efficient photocatalytic hydrogen generation, J. Mater. Chem. A 6 (2018) 11416-11423.

[22] P. Dhiman, G. Rana, A. Kumar, G. Sharma, Dai-Viet N. Vo, M. Naushad, ZnO-based heterostructures as photocatalysts for hydrogen ZnO-based heterostructures as photocatalysts for hydrogen, Environ. Chem. Lett. 20 (2022) 1047-1481.

[23] J. Kegel, I. M. Povey, M. E. Pemble, Zinc oxide for solar water splitting: A brief review of the material's challenges and associated opportunities, Nano Energy 54 (2018) 409-428.

[24] K. M. Lee, C. W. Lai, K. S. Ngai, J. C. Juan, Recent developments of zinc oxide based photocatalyst in water treatment technology: A review, Water Res. 88 (2016) 428-448.

[25] A. Hezam, Q. A. Drmosh, D. Ponnamma, M. A. Bajiri, M.Qamar, K. Namratha, M. Zare, M. B. Nayan, S.A. Onaizi, and K. Byrappa, Strategies to Enhance ZnO Photocatalyst's Performance for Water Treatment: A Comprehensive Review, Chem. Rec. (2022).

[26] S. Kumar, A. Kumar, A. Kumar & V. Krishnan, Nanoscale zinc oxide-based heterojunctions as visible light active photocatalysts for hydrogen energy and environmental remediation, Catal. Rev. (2019) 346-405.

[27] M. Samadi, M. Zirak, A. Naseri, E. Khorashadizade, A. Z. Moshfegh, Recent progress on doped ZnO nanostructures for visible-light photocatalysis, Thin Solid Films 605 (2016) 2-19.

[28] C. Acar, I. Dincer and C. Zamfirescu, A review on selected heterogeneous photocatalysts for hydrogen production, Int. J. Energy Res. 38 (2014) 1903-1920.

[29] S. Goktas, A. Goktas, A comparative study on recent progress in efficient ZnO based nanocomposite and heterojunction photocatalysts: A review, J. Alloys Compd. 863 (2021) 158734.

[30] I. Ahmad, M. S. Akhtar, E. Ahmed, E. Ahmed, M. Y. Naz, Lu modified ZnO/CNTs composite: A promising photocatalyst for hydrogen evolution under visible light illumination, J. Colloid Interface Sci. 584 (2021) 182-192.

[31] I. Ahmad, M. S. Akhtar, M. F. Manzoor, M. Wajid, M. Noman, E. Ahmed, M.Ahmad, W. Q. Khan, A. M. Rana, Synthesis of yttrium and cerium doped ZnO nanoparticles as highly inexpensive and stable photocatalysts for hydrogen evolution, J. Rare Earths (2021) 440-445.

[32] J. Nuñ̃ez, J. Nuñ̃ez, A. E. Platero-Prats, P. Jana, José L. G. Fierro, J. L. G. Fierro, J. L. G. Fierro, and V. A. de la P. O'Shea, Ga-Promoted Photocatalytic H2 Production over Pt/ZnO Nanostructures, ACS Appl. Mater. Interfaces 8 (2016) 23729-23738.

[33] I. Ahmad, S. Shukrullah, M. Y. Naz, M. Ahmad, E. Ahmed, M. S. Akhtar, S. U. Rehman, M. M. Makhlouf, Efficient hydrogen evolution by liquid phase plasma irradiation over Sn doped ZnO/CNTs photocatalyst, Int. J. Hydrog. Energy 46 (2021) 30019-30030.

[34] Z. Hou, X. Zou, X. Pu, L. Wang, Y. Geng, Facile synthesis and improved photocatalytic H2 production of ZnO/Zn$_2$GeO$_4$ and ZnO/Zn$_2$GeO$_4$-Cu composites, J. Solid State Chem. 296 (2021).

[35] D. Bao, P. Gao, X. Zhu, S. Sun, Y. Wang, X. Li, Y. Chen, H. Zhou, Y. Wang, and P. Yang, ZnO/ZnS Heterostructured Nanorod Arrays and Their Efficient Photocatalytic Hydrogen Evolution, Chem. Eur. J. 21 (2015) 12728-12734.

[36] R. Kate, S. Khore, R. Chauhan, U. Kawade, S. Naik, B. Kale, S. Apte, Solid state low temperature synthesis approach for ZnO-ZnS nanoheterostructure with functionality as a photocatalyst for H_2 production and for DSSC, J. Alloys Compd. 858 (2021).

[37] A. Wu, L. Jing, J. Wang, Y. Qu, Y. Xie, B. Jiang, C. Tian, & H. Fu, ZnO-dotted porous ZnS cluster microspheres for high efficient, Pt-free photocatalytic hydrogen evolution, Sci. Rep. 5 (2015).

[38] J. Wang, G. Wang, J. Jiang, Z. Wan, Y. Su, H. Tang, Insight into charge carrier separation and solar-light utilization: rGO decorated 3D ZnO hollow microspheres for enhanced photocatalytic hydrogen evolution, J. Colloid Interface Sci. 564 (2020) 322-332.

[39] Z. Li, D. Jin, Z. Wang, ZnO/CdSe-diethylenetriamine nanocomposite as a step-scheme photocatalyst for photocatalytic hydrogen evolution, Appl. Surf. Sci. 429 (2020).

[40] X. Wang, G. Liu, L. Wang, Z. Chen, G. Q. Lu, and H. Cheng, ZnO–CdS@Cd Heterostructure for Effective Photocatalytic Hydrogen Generation, Adv. Energy Mater. 2 (2012) 42-46.

[41] R. Kalia, Pushpendra, R. K. Kunchala, S.N. Achary, B. S. Naidu, New insights on photocatalytic hydrogen evolution of $ZnFe_{2-x}Ga_xO_4$ ($0 \leq x \leq 2$) solid solutions: Role of oxygen vacancy and ZnO segregated phase, J. Alloys Compd. 875 (2021).

[42] H. Yang, H. Yang, M. Li, X. Liu, X. Liu, X. Liu, Q. Ge, and H. Wang, Hollow Au-ZnO/CN Nanocages Derived from ZIF-8 for Efficient Visible-Light-Driven Hydrogen Evolution from Formaldehyde Alkaline Solution, Eur. J. Inorg. Chem. (2019) 2761-2767.

[43] S. Khan, M. Je, N. N. T. Ton, W. Lei, T. Taniike, S. Yanagida, Chiaki Terashima, A. Fujishima, H. Choi, K. Katsumata, C-doped ZnS-ZnO/Rh nanosheets as multijunctioned photocatalysts for effective H_2 generation from pure water under solar simulating light, Appl. Catal. B 297 (2021).

[44] Y. Piña-Pérez, O. Aguilar-Martínez, P. Acevedo-Peña, C.E. Santolalla-Vargas, S. Oros-Ruíz, F. Galindo-Hernández, R. Gómez, F. Tzompantzi, Novel ZnS-ZnO composite synthesized by the solvothermal method through the partial sulfidation of ZnO for H_2 production without sacrificial agent, Appl. Catal. B 230 (2018) 125-134.

[45] A. Irshad, A. Ejaz, M. Ahmad, M. S. Akhtar, M. A. Basharat, W. Q. Khan, M. I. Ghauri, A. Ali, M. F. Manzoor, The investigation of hydrogen evolution using Ca doped ZnO catalysts under visible light illumination, Mater. Sci. Semicond. Process. 105 (2020).

[46] Y. Chang, S. Syu, Z. Wu, Fabrication of $ZnO-In_2S_3$ composite nanofiber as highly efficient hydrogen evolution photocatalyst, Mater. Lett. 302 (2021).

[47] Y. Zhao, Y. Guo, J. Li, P. Li, Efficient hydrogen evolution with ZnO/SrTiO$_3$ S-scheme heterojunction photocatalyst sensitized by Eosin Y, Int. J. Hydrog. Energy 46 (2021) 18922-18935.

[48] Z. Li, W. Zhang, Q. Zhao, H. Gu, Y. Li, G. Zhang, F. Zhang, and X. Fan, Eosin Y Covalently Anchored on Reduced Graphene Oxide as an Efficient and Recyclable Photocatalyst for the Aerobic Oxidation of α-Aryl Halogen Derivatives, ACS Sustainable Chem. Eng. 3 (2015) 468-474.

[49] T. Yeh, J. Cihla´r, C. Chang, C. Cheng and H. Teng, Roles of graphene oxide in photocatalytic water splitting, Materials Today 16 (2013) 78-84.

[50] R. Gang, L. Xu, Y. Xia, L. Zhang, S. Wang, and R. Li, Facile One-step Production of 2D/2D ZnO/rGO Nanocomposites under Microwave Irradiation for Photocatalytic Removal of Tetracycline, ACS Omega 6 (2021) 3831-3839.

[51] K. Lu, Y. Li, Z. Tang, and Y. Xu, Roles of Graphene Oxide in Heterogeneous Photocatalysis, ACS Mater. Au 1 (2021) 37-54.

[52] D. Popugaeva, T. Tian, A. K. Ray, Hydrogen production from aqueous triethanolamine solution using Eosin Y-sensitized ZnO photocatalyst doped with platinum, Int. J. Hydrog. Energy 45 (2020) 11097-11107.

[53] A. Lewandowska-Andrałojc, D. Larowska, E. Gacka, T. Pedzinski, and B. Marciniak, How Eosin Y/Graphene Oxide-Based Materials Can Improve Efficiency of Light-Driven Hydrogen Generation: Mechanistic Aspects, J. Phys. Chem. C 124 (2020) 2747-2755.

[54] Z. Jin, Y. Li, X. Hao, Ni, Co-Based Selenide Anchored g-C$_3$N$_4$ for Boosting Photocatalytic Hydrogen Evolution, Acta Phys. -Chim. Sin. 37 (**10**) (2021) 1912033.

[55] Y. Lou, Y. Zhang, L. Cheng, J. Chen, and Y. Zhao, A Stable Plasmonic Cu@Cu$_2$O/ZnO Heterojunction for Enhanced Photocatalytic H$_2$ Generation, ChemSusChem (2018).

[56] S. Kumar, N. L. Reddy, A. Kumar, M. V. Shankar, V. Krishnan, Two-dimensional N-doped ZnO-graphitic carbon nitride nanosheets heterojunctions with enhanced photocatalytic hydrogen evolution, Int. J. Hydrog. Energy 43 (2018) 3988-4002.

[57] H. Mou, C. Song, Y. Zhou, B. Zhang, D. Wang, Design and synthesis of porous Ag/ZnO nanosheets assemblies as super photocatalysts for enhanced visible-light degradation of 4-nitrophenol and hydrogen evolution, Appl. Catal. B 221 (2018) 565-573.

[58] Z. Guan, P. Wang, Q. Li, Y. Li, X. Fu, J. Yang, Remarkable enhancement in solar hydrogen generation from MoS$_2$-RGO/ZnO composite photocatalyst by constructing a robust electron transport pathway, Chem. Eng. J. 327 (2017) 397-405.

[59] F. Chen, L. Zhang, X. Wang, R. Zhang, Noble-metal-free NiO@Ni-ZnO/reduced graphene oxide/CdS heterostructure for efficient photocatalytic hydrogen generation, Appl. Surf. Sci. 2017 (2017) 962-969.

[60] X. Wang, Q. Li, H. Xu, L. Gan, X. Ji, H. Liu, R. Zhang, CuS-modified ZnO rod/reduced graphene oxide/CdS heterostructure for efficient visible-light photocatalytic hydrogen generation, Int. J. Hydrog. Energy 45 (2020) 28394-28403.

[61] E. Hong, J. H. Kim, Oxide content optimized ZnS-ZnO heterostructures via facile thermal treatment process for enhanced photocatalytic hydrogen production, Int. J. Hydrog. Energy 39 (2014) 9985-9993.

[62] T. P. Yendrapati, A. Gautam, S. Bojja, U. Pal, Formation of ZnO@CuS nanorods for efficient photocatalytic hydrogen generation, Sol Energy 196 (2020) 540-548.

[63] G. Zhou, X. Xu, T. Ding, B. Feng, Z. Bao, and J. Hu, Well−Steered Charge−Carrier Transfer in 3D Branched Cu_xO/ZnO@Au Heterostructures for Efficient Photocatalytic Hydrogen Evolution, ACS Appl. Mater. Interfaces 7 (2015) 26819-26827.

[64] V. Vaiano, G. Iervolino, L. Rizzo, Cu-doped ZnO as efficient photocatalyst for the oxidation of arsenite to arsenate under visible light, Appl. Catal. B 238 (2018) 471-479.

[65] S. Chabri, A. Dhara, B. Show, D. Adak, A. Sinha and N. Mukherjee, Mesoporous CuO–ZnO p–n heterojunction based nanocomposites with high specific surface area for enhanced photocatalysis and electrochemical sensing, Catal. Sci. Technol. 6 (2016) 3238-3252.

[66] T. P. Y. Taraka, A. Gautam, S. L. Jain, S. Bojja, U. Pal, Controlled addition of Cu/Zn in hierarchical CuO/ZnO p-n heterojunction photocatalyst for high photoreduction of CO2 to MeOH, J. CO2 Util. 31 (2019) 207-214.

[67] Mohammed Abdullah Bajiri, Abdo Hezam, K. Namratha, R. Viswanath, Q.A. Drmosh, H.S. Bhojya Naik, K. Byrappa, CuO/ZnO/g-C_3N_4 heterostructures as efficient visible light-driven photocatalysts, J. Environ. Chem. Eng. 7 (2019) 103412.

[68] Y. Wang, H. Ping, T. Tan, W. Wang, P. Ma, H. Xie, Enhanced hydrogen evolution from water splitting based on ZnO nanosheet/CdS nanoparticle heterostructures, RSC Adv. 9 (2019) 28165-28170.

[69] M. Niederberger and G. Garnweitner, Nonaqueous Synthesis of Barium Titanate Nanocrystals in Acetophenone as Oxygen Supplying Agent, MRS Online Proceedings Library 879 (2005).

[70] Nillohit Mukherjee, Sk. Faruque Ahmed, Kalyan Kumar Chattopadhyay, Anup Mondal, Role of solute and solvent on the deposition of ZnO thin films, Electrochim. Acta 54 (2009) 4015-4024.

[71] M. Niederberger and G. Garnweitner, Organic Reaction Pathways in the Nonaqueous Synthesis of Metal Oxide Nanoparticles, Chem. Eur. J. 12 (2006) 7282-7302.

[72] N. Pinna and M. Niederberger, Surfactant-Free Nonaqueous Synthesis of Metal Oxide Nanostructures, Angew. Chem. Int. Ed. 47 (2008) 5292-5304.

[73] I. Pastoriza-Santos and L. M. Liz-Marza´n, N,N-Dimethylformamide as a Reaction Medium for Metal Nanoparticle Synthesis, Adv. Funct. Mater. 19 (2009) 679-688.

[74] X. Tang, X. Li, Z. Cao, J. Yang, H. Wang, X. Pu, Z. Yu, Synthesis of graphene decorated with silver nanoparticles by simultaneous reduction of graphene oxide and silver ions with glucose, Carbon 59 (2013) 93-99.

[75] I. Bilecka, I. Djerdj, M. Niederberger, One-minute synthesis of crystalline binary and ternary metal oxide nanoparticles, Chem. Commun. (2008) 886-888.

[76] B. H. Park, H. Park, T. Kim, S. J. Yoon, Y. Kim, N. Son, M. Kang, S-scheme assisted Cu_2O/ZnO flower-shaped heterojunction catalyst for breakthrough hydrogen evolution by water splitting, Int. J. Hydrog. Energy (2021).

[77] M. Sˇcepanovi´c, M. Grujic-Broj´cin, K. Vojisavljevic, S. Bernik and T. Sreckovi´c, aman study of structural disorder in ZnO nanopowders, J. Raman Spectrosc. 41 (2010) 914-921.

[78] G. Xiong, U. Pal, J. Garcia Serrano, Correlations among size, defects, and photoluminescence in ZnO nanoparticles, J. Appl. Phys. 101 (2007) 024317.

[79] Y. Wang, W. Ruan, J. Zhang, B. Yang, W. Xu, B. Zhao, J. R. Lombardi, Direct observation of surface-enhanced Raman scattering in ZnO nanocrystals, J. Raman Spectrosc. 1077 (2009) 1072.

[80] H. Solache-Carranco, G. Jua´rez-Dı´az, A. Esparza-Garcı´a, M. Brisen˜o-Garcı´a, M. Galva´n-Arellano, J. Martı´nez-Jua´rez, G. Romero-Paredes, R. Pen˜a-Sierra, Photoluminescence and X-ray diffraction studies on Cu2O, J. Lumin. 129 (2009) 1483-1487.

[81] C. K. King'ondu, A. Iyer, E. C. Njagi, N. Opembe, H. Genuino, H. Huang, R. A. Ristau, S. L. Suib, Light-Assisted Synthesis of Metal Oxide Hierarchical Structures and Their Catalytic Applications, J. Am. Chem. Soc. 133 (2011) 4186-4189.

[82] O. Dobrozhan, A. Opanasyuk, M. Kolesnyk, M. Demydenko, and H. Cheong, Substructural investigations, Raman, and FTIR spectroscopies of nanocrystalline ZnO films deposited by pulsed spray pyrolysis, Phys. Status Solidi A 212 (2015) 2915-2921.

[83] S. Sivasakthi, K. Gurunathan, Graphitic carbon nitride bedecked with CuO/ZnO hetero-interface micro flower towards high photocatalytic performance, Renew. Energy 159 (2020) 786-800.

[84] A. A. Bayode, E. M. Vieira, R. Moodley, S. Akpotu, A.S. S. Camargo, D. Fatta-Kassinos, E. I. Unuabonah, Tuning ZnO/GO p-n heterostructure with carbon interlayer supported on clay for visible-light catalysis: Removal of steroid estrogens from water, Chem. Eng. J. 420 (2021) 127668.

[85] H. Asgar, K. M. Deen, W. Haider, Estimation of electrochemical charge storage capability of ZnO/CuO/reduced graphene oxide nanocomposites, Int J Energy Res. 44 (2020) 1580-1593.

[86] P. Kumar, S. Som, M. K. Pandey, S. Das, A. Chanda, J. Singh, Investigations on optical properties of ZnO decorated graphene oxide (ZnO@GO) and reduced graphene oxide (ZnO@r-GO), J. Alloys Compd. 744 (2018) 64-74.

[87] P. Zhu, M. Duan, R. Wang, J. Xu, P. Zou, H. Jia, Facile synthesis of ZnO/GO/Ag$_3$PO$_4$ heterojunction photocatalyst with excellent photodegradation activity for tetracycline hydrochloride under visible light, Colloids Surf. A: Physicochem. Eng. Asp. 602 (2020) 125118.

[88] X. Di, F. Guo, Z. Zhu, Z. Xu, Z. Qian, Q. Zhang, In situ synthesis of ZnO–GO/CGH composites for visible light photocatalytic degradation of methylene blue, RSC Adv. 9 (2019) 41209-51217.

[89] J. M. Jacob, R. Rajan, M. Aji, G. G. Kurup, A. Pugazhendhi, Bio-inspired ZnS quantum dots as efficient photocatalysts for the degradation of methylene blue in aqueous phase, Ceram. Int. 45 (2019) 4857-4862.

[90] V. Sabaghi, F. Davar, Z. Fereshteh, ZnS nanoparticles prepared via simple reflux and hydrothermal method: Optical and photocatalytic properties, Ceram. Int. 44 (2018) 7545-7556.

[91] T. Wang, B. Jin, Z. Jiao, G. Lu, J. Ye, Y. Bi, Photo-directed growth of Au nanowires on ZnO arrays for enhancing photoelectrochemical performances, J. Mater. Chem. A 2 (2014) 15553-15559.

[92] Y. Zhu, Z.i Xu, K. Yan, H. Zhao, J. Zhang, One-Step Synthesis of CuO−Cu$_2$O Heterojunction by Flame Spray Pyrolysis for Cathodic Photoelectrochemical Sensing of L-Cysteine, ACS Appl. Mater. Interfaces 9 (2017) 40452-40460.

[93] L. Xu, J. Li, H. Sun, X. Guo, J. Xu, H. Zhang, X. Zhang, In situ Growth of Cu$_2$O/CuO Nanosheets on Cu Coating Carbon Cloths as a Binder-Free Electrode for Asymmetric Supercapacitors, Front. Chem. 7 (2019).

[94] L. Chen, Z. Xu, J. Li, B. Zhou, M. Shan, Y. Li, L. Liu, B. Li, J. Niu, Modifying graphite oxide nanostructures in various media by high-energy irradiation, RSC Adv. 4 (2014) 1025-1031.

[95] Z. Li, Y. Wang, Y. Chen, M. Wu, Controllable growth of MnO$_x$ dual-nanocrystals on N-doped graphene as lithium-ion battery anode, RSC Adv. 7 (2017) 6396-6402.

[96] S. Adhikari, D. Sarkar, G. Madras, Hierarchical Design of CuS Architectures for Visible Light Photocatalysis of 4-Chlorophenol, ACS Omega 2 (2017) 4009-4021.

[97] D. Bui, M. Pham, H. Tran, T. Nguyen, T. M. Cao, V. V. Pham, Revisiting the Key Optical and Electrical Characteristics in Reporting the Photocatalysis of Semiconductors, ACS Omega 6 (2021) 27379-27386.

[98] H. Huang, X. Li, X. Han, N. Tian, Y. Zhang and T. Zhang, Moderate band-gap-broadening induced high separation of electron–hole pairs in Br substituted BiOI: a combined experimental and theoretical investigation, Phys.Chem.Chem.Phys. 17 (2015) 3673-3679.

[99] J. Mooney, P. Kambhampati, Get the Basics Right: Jacobian Conversion of Wavelength and Energy Scales for Quantitative Analysis of Emission Spectra, J. Phys. Chem. Lett. 4 (2013) 3316-3318.

[100] Y. Zhu, C. Sow, T. Yu, Q. Zhao, P. Li, Z. Shen, D. Yu, and J. T. Thong, Co-synthesis of ZnO–CuO Nanostructures by Directly Heating Brass in Air, Adv. Funct. Mater. 16 (2006) 2415-2422.

[101] P. Chand, Manisha, P. Kumar, Effect of precursors medium on structural, optical and dielectric properties of CuO nanostructures, Optik 156 (2018) 743-753.

[102] H. Siddiqui, M.S. Qureshi, F. Z. Haque, Surfactant assisted wet chemical synthesis of copper oxide (CuO) nanostructures and their spectroscopic analysis, Optik 127 (2016) 2740-2747.

[103] R. M. Mohamed, F. A. Harraz, A. Shawky, CuO nanobelts synthesized by a template-free hydrothermal approach with optical and magnetic characteristics, Ceram. Int. 40 (2014) 2127-2133.

[104] O. Mnethu, S. S. Nkosi, I. Kortidis, D. E. Motaung, R.E. Kroon, Hendrik C. Swart, Napo G. Ntsasa, J. Tshilongo, T. Moyo, Ultra-sensitive and selective p-xylene gas sensor at low operating temperature utilizing Zn doped CuO nanoplatelets: Insignificant vestiges of oxygen vacancies, J. Colloid Interface Sci. 576 (2020) 364-375.

[105] R. Agarwal, K. Verma, N. K. Agrawal, R. K. Duchaniya, R. Singh, Synthesis, characterization, thermal conductivity and sensitivity of CuO nanofluids, Appl. Therm. Eng. 102 (2016) 1024-1036.

[106] Y. G. Wang, S. P. Lau, H. W. Lee, S. F. Yu, and B. K. Tay, X. H. Zhang, H. H. Hng, Photoluminescence study of ZnO films prepared by thermal oxidation of Zn metallic films in air, J. Appl. Phys. 94 (2003) 354.

[107] X. Peng, J. Xu, H. Zang, B. Wang, Z. Wang, Structural and PL properties of Cu-doped ZnO films, J. Lumin. 128 (2008) 297-300.

[108] Y. Joo, J. Wi, W. Lee, Y. Chung, D. Cho, S. Kang, D. Um, and C. Kim, Work Function Tuning of Zinc–Tin Oxide Thin Films Using High-Density O_2 Plasma Treatment, Coatings 10 (2020) 1026.

[109] J. Low, J. Yu, M. Jaroniec, S. Wageh, A. A. Al-Ghamdi, Heterojunction Photocatalysts, Adv. Mater. 29 (2017) 1601694.

[110] Fei He, Aiyun Meng, Bei Cheng, Wingkei Ho, Jiaguo Yu, Enhanced photocatalytic H2-production activity of WO_3/TiO_2 step-scheme heterojunction by graphene modification, Chin. J. Catal. 41 (2020) 9-20.

[111] Q. Luan, Q. Chen, J. Zheng, R. Guan, Y. Fang, and X. Hu, In-situ construction of 2D-ZnS@ZnO Z-scheme heterostructure nanosheet with highly ordered ZnO core and disordered ZnS shell for enhancing the photocatalytic hydrogen evolution, ChemNanoMat 6 (2020) 470.

[112] Y. Xiao, T. Wang, G. Qiu, K. Zhang, C. Xue, B. Li, Synthesis of EDTA-bridged CdS/g-C$_3$N$_4$ heterostructure photocatalyst with enhanced performance for photoredox reactions, J. Colloid Interface Sci. 577 (2020) 459-470.

[113] Y. Shi, X. Lei, L. Xia, Q. Wu, W. Yao, Enhanced photocatalytic hydrogen production activity of CdS coated with Zn-anchored carbon layer, Chem. Eng. J. 393 (2020) 124751.

[114] X. Zhang, W. An, Y. Li, J. Hu, H. Gao, W. Cui, Efficient photo-catalytic hydrogen production performance and stability of a three-dimensional porous CdS NPs-graphene hydrogel, Int. J. Hydrog. Energy 43 (2018) 9902-9913.

[115] Z. B. Yu, Y. P. Xie, G. Liu, G. Q. Lu, X. L. Ma and H. Cheng, Self-assembled CdS/Au/ZnO heterostructure induced by surface polar charges for efficient photocatalytic hydrogen evolution, J. Mater. Chem. A 1 (2013) 2773-2776.

[116] D. Ma, J. Shi, Y. Zou, Z. Fan, X. Ji, and C. Niu, Highly Efficient Photocatalyst Based on a CdS Quantum Dots/ZnO Nanosheets 0D/2D Heterojunction for Hydrogen Evolution from Water Splitting, ACS Appl. Mater. Interfaces 9 (2017) 23577-25386.

[117] X. Wang, G. Liu, Z. Chen, F. Li, L. Wang, G. Q. Lu and H. Cheng, Enhanced photocatalytic hydrogen evolution by prolonging the lifetime of carriers in ZnO/CdS heterostructures, Chem. Commun. (2009) 3452-3454.

[118] G. Sun, B. Xiao, H. Zheng, J. Shi, S. Mao, C. He, Z. Li, Y. Cheng, Ascorbic acid functionalized CdS-ZnO core-shell nanorods with hydrogen spillover for greatly enhanced photocatalytic H_2 evolution and outstanding photostability, J. Mater. Chem. A 9 (2021) 9735-9744.

[119] D. Xiang, X. Hao, and Z. Jin, Cu/CdS/MnO$_x$ Nanostructure-Based Photocatalyst for Photocatalytic Hydrogen Evolution, ACS Appl. Nano Mater. 4 (2021) 13848-13860.

[120] S. Zulfiqar, S. Liu, N. Rahman, H. Tang, S. Shah, X. Yu, Q. Liu, Construction of S-scheme MnO_2@CdS heterojunction with core–shell structure as H_2-production photocatalyst, Rare Met. 40 (**9**) (2021) 2381-2391.

[121] S. Dhingra, T. Chhabra, V. Krishnan, and C. M. Nagaraja, Visible-Light-Driven Selective Oxidation of Biomass-Derived HMF to DFF Coupled with H_2 Generation by Noble Metal-Free $Zn_{0.5}Cd_{0.5}S/MnO_2$ Heterostructures, ACS Appl. Energy Mater. 3 (2020) 7138-7148.

[122] D. You, C. Xu, J. Wang, W. Su, F. Qin, and Y. Liu, Three-Dimensional Core−Shell Nanorod Arrays for Efficient Visible Light Photocatalytic H_2 Production, ACS Appl. Mater. Interfaces 10 (2018) 35184-35193.

[123] A. Raza, H. Shen, A. A. Haidry, Novel $Cu_2ZnSnS_4/Pt/g-C_3N_4$ heterojunction photocatalyst with straddling band configuration for enhanced solar to fuel conversion, Appl. Catal. B 277 (2020) 119239.

[124] J. Schneider and D. W. Bahnemann, Undesired Role of Sacrificial Reagents in Photocatalysis, J. Phys. Chem. Lett. 4 (2013) 3479-3483.

[125] D. V. Markovskaya, S. V. Cherepanova, E. Y. Gerasimov, A. V. Zhurenok, A. V. Selivanova, D. S. Selishchev and E. A. Kozlova, The influence of the sacrificial agent nature on transformations of the $Zn(OH)_2/Cd_{0.3}Zn_{0.7}S$ photocatalyst during hydrogen production under visible light, RSC Adv. 10 (2020) 1341.

[126] Y. V. Kuznetsova and A. A. Rempel, Size and Zeta Potential of CdS Nanoparticles in Stable Aqueous Solution of EDTA and NaCl, Inorg. Mater. 51 (2015) 215-219.

[127] L. Cui, Y. Wang, L. Gao, L. Hu, L. Yan, Q. Wei, B. Du, EDTA functionalized magnetic graphene oxide for removal of Pb(II), Hg(II) and Cu(II) in water treatment: Adsorption mechanism and separation property, Chem. Eng. J. 281 (2015) 1-10.

[128] F. Demoisson, R. Piolet, and F. Bernard, Hydrothermal Synthesis of ZnO Crystals from Zn(OH)2 Metastable Phases at Room to Supercritical Conditions, Cryst. Growth Des. 14 (2014) 5388-5396.

[129] S.V. Nistor, D. Ghica, M. Stefan, I. Vlaicu, J.N. Barascu, C. Bartha, Magnetic defects in crystalline Zn(OH)2 and nanocrystalline ZnO resulting from its thermal decomposition, J. Alloys Compd. 548 (2013) 222-227.

[130] S. Luo, R. Chen, L. Xiang, and J. Wang, Hydrothermal Synthesis of (001) Facet Highly Exposed ZnO Plates: A New Insight into the Effect of Citrate, Crystals 9 (2019) 552.

[131] C. Xing, H. Kai, W. Chengyan, Preparation of flaky dihydrate zinc oxalate particles by controlled chelating double-jet precipitation, Adv. Powder Technol. 30 (9) (2019) 1941-1949.

[132] P. Zhang, X. Li, Q. Zhao, and S. Liu, Synthesis and optical property of one-dimensional spinel ZnMn2O4 nanorods, Nanoscale Res. Lett. 6 (2011) 323.

[133] Y. Li, X. Zhou, Y. Xing, In situ thermal-assisted loading of monodispersed Pt nanoclusters on CdS nanoflowers for efficient photocatalytic hydrogen evolution, Appl. Surf. Sci. 506 (2020) 144933.

[134] A. Ramos-Corona, R. Rangel, J. Lara, R. Trejo-Tzab, P. Bartolo and J. J. Alvarado-Gil, Novel nitrogen plasma doping on CdS/GO compounds and their photocatalytic assessment, Nanotechnology 33 (2022) 055705.

[135] A. V. Moholkar, G.L. Agawane, Kyu-Ung Sim, Ye-bin Kwon, Doo Sun Choi, K.Y. Rajpure, J.H. Kim, Temperature dependent structural, luminescent and XPS studies of CdO:Ga thin films deposited by spray pyrolysis, J. Alloys Compd. 506 (2010) 794-799.

[136] P. W. Menezes, A. Indra, V. Gutkin and M. Driess, Boosting electrochemical water oxidation through replacement of O h Co sites in cobalt oxide spinel with manganese, Chem. Commun. 53 (2017) 8018.

[137] C. Shamitha, T. Senthil, L. Wu, B. S. Kumar, S. Anandhan, Sol–gel electrospun mesoporous $ZnMn_2O_4$ nanofibers with superior specific surface area, J. Mater. Sci.: Mater Electron. 28 (2017) 15846-15860.

[138] Z. K. Heiba, M. B. Mohamed, S. I. Ahmed, Modifying the structure and optical characteristics of $ZnMn_2O_4$ by alloying with CdS to form heterostructure nanocomposite, Appl. Phys. A 127 (2021) 883.

[139] Z. Ma, F. Li, A. Jia, X. Zhang, Y. Wang, Facile synthesis of EDTA grafted 3D spherical-chain porous silica with high capacity for rapidly selective adsorption of Cu(II) from aqueous solutions, J. Porous Mater. 28 (2021) 299-301.

[140] N. Nwaji, E. M. Akinoglu, B. Lin, X. Wang, and M. Giersig, One-Pot Synthesis of One-Dimensional Multijunction Semiconductor Nanochains from Cu1.94S, CdS, and ZnS for Photocatalytic Hydrogen Generation, ACS Appl. Mater. Interfaces, 13 (2021) 58630-58639.

[141] D. Q. Dao, T. K. A. Nguyen, S. G. Kang, and E. W. Shin, Engineering Oxidation States of a Platinum Cocatalyst over Chemically Oxidized Graphitic Carbon Nitride Photocatalysts for Photocatalytic Hydrogen Evolution, ACS Sustainable Chem. Eng. 9 (2021) 14537-14549.

[142] W. Zhong, X. Wu, P. Wang, J. Fan, and H. Yu, Homojunction CdS Photocatalysts with a Massive $S_2{}^-$-Adsorbed Surface Phase: One-Step Facile Synthesis and High H_2-Evolution Performance, ACS Sustainable Chem. Eng. 8 (2020) 543-551.

[143] F. Dong, Z. Zhao, T. Xiong, Z. Ni, W. Zhang, Y. Sun, and W. Ho, In Situ Construction of g-C_3N_4/g-C_3N_4 Metal-Free Heterojunction for Enhanced Visible-Light Photocatalysis, ACS Appl. Mater. Interfaces 5 (2013) 11392-11401.

[144] T. K. A. Nguyen, T. Pham, H. Nguyen-Phu, E. W. Shin, The effect of graphitic carbon nitride precursors on the photocatalytic dye degradation of water-dispersible graphitic carbon nitride photocatalysts, Appl. Surf. Sci. 537 (2021) 148027.

UNIVERSITY OF ULSAN

SCHOOL OF CHEMICAL ENGINEERING

————————oOo————————

MASTER'S THESIS

MODIFIED ELECTRONIC STRUCTURE OF ZINC OXIDES FOR PHOTOCATALYTIC HYDROGEN EVOLUTION

Student   **:**   **VUONG HOAI THANH**

Student ID   **:**   **20205801**

Supervisor   **:**   **Prof. Jin Suk Chung, Ph.D**

ULSAN CITY, REPUBLIC OF KOREA, MAY 2022